

Stochastic coupling of solar photosphere and corona

Vadim M. Uritsky

Catholic University of America at NASA Goddard Space Flight Center, Greenbelt, MD 20771 USA

`vadim.uritsky@nasa.gov`

Joseph M. Davila

NASA Goddard Space Flight Center, Greenbelt, MD 20771 USA

Leon Ofman

Catholic University of America at NASA Goddard Space Flight Center, Greenbelt, MD 20771 USA

Aaron J. Coyner

University of Tulsa, Tulsa, OK 74104 USA

ABSTRACT

It is commonly believed that the observed solar activity is driven by the dissipation of free (nonpotential) magnetic energy injected into the corona by dynamic processes in the photosphere. The enormous range of scales involved in the solar activity makes it difficult to track down the photospheric origin of each coronal dissipation event, especially in the presence of complex magnetic topologies. In this paper, we propose a new statistical-physical approach for testing the photosphere-corona coupling as manifested in a quiet solar region. We investigate large ensembles of photospheric and coronal events detected in co-aligned sets of images provided respectively by SOHO MDI and STEREO EUVI instruments. We show that for properly adjusted detection thresholds corresponding to the same degree of intermittency in the photosphere and corona, the detected events are described by similar occurrence probability distributions of time-integrated quantities but significantly different geometric properties. We derive a set of scaling relations reconciling these empirical results and enabling statistical forecast of coronal dynamics based on photospheric measurements. The perform analysis suggests that multiscale energy dissipation in the corona is directly controlled by the turbulent photospheric convection so that probabilistic properties of energy release events in the photosphere are imprinted in the corona. The nonlocal nature of the photospheric network makes this coupling essentially nonlocal and non-deterministic. Our results are in agreement with the Parker's coupling scenario in which random photospheric shuffling generates marginally stable magnetic discontinuities at the coronal level, and are also consistent with an impulsive wave heating involving multiscale Alfvénic wave packets. More research is needed to tell the two mechanisms apart.

Subject headings: Sun: activity – Sun: magnetic fields – complexity

1. Introduction

The Sun is an inherently complex and multiscale system which continues to challenge the-

orists and experimentalists alike. Coronal holes with scales typically on the order of a solar radius are the sources of high speed solar wind streams. Coronal active region magnetic loops, with char-

acteristic scales of 10,000 km, exhibit somewhat steady heating. Direct current heating of the coronal plasma, unresolved with present instruments, takes place at a typical ohmic dissipation scale in the corona, which is likely to be as small as 100 km. The Sun also exhibits a broad range of temporal scales. The largest features are observed to last for months. Coronal holes and coronal streamers can persist for several 27-day solar rotations with little change, while M- and X-class solar flares release a vast amount of energy essentially doubling the solar luminosity for a brief period of a few minutes (see e.g. Aschwanden 2006; Solanki et al. 2006, and references therein).

Despite the enormous complexity of solar photosphere and corona, the fundamental underlying process controlling their interaction could be surprisingly simple. It is widely believed that the ultimate power source for all energy release processes in the upper solar atmosphere is the convection at the solar surface mediated by magnetic field. The observed solar activity is likely to be driven by the dissipation of free (nonpotential) magnetic energy which is injected into the corona due to a variety of processes in the photosphere (Klimchuk 2006). Among the most important such processes are the injection of helicity associated with new magnetic structures (Falconer et al. 2008; Abramenko & Yurchyshyn 2010; McAteer et al. 2010; Conlon et al. 2010) and the fragmentation of the existing magnetic flux subject to magnetic footpoint shuffling due to the turbulent photospheric convection (Lamb et al. 2008; Chaouche et al. 2011; Abramenko 2005). The amount of free coronal magnetic energy supplied through these processes seems to be in a quasi-steady balance with the energy released via coronal heating and flaring activity (Simon et al. 2001).

Although the convective scenario of the photosphere - corona coupling has been reproduced in numerical simulations, its empirical verification presents a significant challenge. The broad ranges of scales involved in solar activity makes it impossible to track the photospheric origin of each particular coronal dissipation event, especially of the events associated with complex multiscale magnetic topologies (e.g., Antiochos 1998; Antiochos et al. 2007; Schrijver et al. 1992; Balke et al. 1993; Lawrence et al. 1993; Abramenko et al.

2002; Georgoulis 2005; McAteer et al. 2010; Parnell et al. 2009; Uritsky & Davila 2012). Coronal brightenings occurring on strongly entangled magnetic field lines tend to interact in a nonlinear fashion producing vast regions of secondary instabilities in response to relatively small triggers (Klimchuk 2006; Fuentes & Klimchuk 2010). The bulk of the emitting coronal plasma is not steady but is rather dynamic and constantly evolving (Vial & Klimchuk 2011, 2012). Turbulent behavior of high-Reynolds number photospheric flows (Abramenko et al. 2002) as well as turbulence and fractal diffusion in the corona (Berghmans et al. 1998; Uritsky et al. 2007, 2009; Aschwanden 2012a) further increases the complexity of the coupling between the two solar regions. In addition, a noticeable fraction of magnetic discontinuities created by the photospheric motion is likely to remain silent until a local plasma instability condition is met (Vlahos & Georgoulis 2004; Aschwanden 2006).

Based on this picture, the coronal response to a single reconfiguration of the photospheric field is likely to be nonlocal, non-simultaneous, and energetically disproportional to the triggering photospheric event when investigated on a case-by-case basis. Searching for driving signatures of individual coronal brightenings in relatively stationary quiet solar regions can be particularly difficult, while finding deterministic cause and effect links governing an ensemble of such events is close to impossible.

In this paper, we adopt a different strategy focusing on statistical-physical signatures of photospheric and coronal events occurring in a quiet Sun. We consider two types of events – photospheric magnetic field enhancements and coronal heating events observed simultaneously within the same solar region. The events are detected by thresholding SOHO MDI line of sight photospheric magnetograms and STEREO EUVI coronal emission images, correspondingly. The events represent intermittent conditions in the photosphere and corona, with the net area covered by the events at any given time being less than five percent of the total image area.

The results of our analysis show that for the detection thresholds leading to same degree of intermittency of the photospheric and coronal events, they are described by nearly identical power-law

probability distributions of event areas, spatiotemporal volumes, and integrated intensities. The power-law distribution exponents characterizing solar photosphere and corona undergo similar variations during the studied 14-hour interval. The statistical signatures obtained suggest that temporal and spatial scales of coronal heating events can be directly controlled by convective shuffling motions of the photospheric magnetic field. The results are in agreement with the Parker’s coupling scenario in which multiscale photospheric flows generate a large amount of marginally stable magnetic structures at the coronal level, the free magnetic energy stored by the structures being to a large extent predefined by the photospheric motion (Parker 1983, 1988). The coronal brightenings release the energy of a random subset of these magnetic discontinuities repeating their probabilistic pattern. Alternatively, the results can indicate that the photospheric dynamics generates a broad-band spectrum of Alfvén waves transmitted into the chromosphere and eventually into the corona (e.g., Davila 1987; Ofman et al. 1998; Kudoh & Shibata 1999; De Pontieu et al. 2007). In either case, our observations suggest strong energy coupling between ensemble-based properties of solar photosphere and corona – the effect we refer to as *stochastic coupling*.

2. Methods and results

We have studied simultaneously collected sets of SOHO MDI line of sight (LOS) magnetograms (Scherrer et al. 1995) and STEREO-B EUVI images (Howard et al. 2008) showing the dynamics of a quiet Sun during 17:29:00 04/05/2007 - 10:58 04/06/2007. The images were preprocessed and derotated using the standard Solar Soft software. STEREO EUVI images were rebinned to down to the spatial resolution of SOHO MDI data (0.6 arcsec, or about 0.44 Mm) and interpolated in time using linear interpolation scheme to match the timing of the nearest MDI snapshot. To reduce the influence of the granulation noise (DeForest et al. 2007; Lamb et al. 2008) the images were also smoothed in time using a 5 minute boxcar moving window. The obtained data cubes contained $770 \times 500 \times 952$ data points in the latitudinal, longitudinal and temporal directions, correspondingly. As a result of the described co-alignment procedures, both data sets (MDI and

EUVI) were described by the same sets of heliographic positions and times.

Fig. 1 shows full-disk SOHO MDI and STEREO EUVI images with the studied field of view (FoV) outlined by the white frame. The overall solar activity level remained very low, with the GOES X-ray fluxes staying below 10^{-8} W m^{-2} . Two decaying active regions, NOAA 10949 and NOAA 10950, were seen outside of the FoV; neither of them produced solar flares starting from several days before till several days after the studied time interval. The position of the FoV close to the disk center ensures small projection distortions. The latitudinal size of the region (about one fourth of the visible solar diameter) is sufficiently large to obtained statistically representative measures of the photosphere - corona interaction.

The magnetic network and coronal emission pattern of the studied region are typical of a quiet Sun (Fig. 2). The LOS magnetic field features a hierarchy of spatial scales representing several levels of photospheric granulation with a roughly uniform distribution of large-scale magnetic flux across the FoV. The imbalance between positive and negative fluxes is about 15% of the total unsigned flux in this region, with the prevalence of the negative flux. The EUVI emission field exhibits a diffuse, fractal-like spatial distribution of intensity characteristic of a nonflaring corona. Some of the bright coronal regions coincide with mixed-polarity magnetic regions, in agreement with earlier studies of the quiet Sun magnetic network (see e.g. Falconer et al. 1998). The appearance of bright coronal points in the vicinity of magnetic field reversals can be a signature of low-altitude magnetic reconnection occurring on magnetic discontinuities driven by the photospheric motion (see Aschwanden 2006, chap. 10 for a review).

To study the dynamics of photospheric magnetic field and coronal emission flux, we applied the same numerical approach which enabled a detection of spatiotemporal intermittent events in each data sets. The approach is based on spatiotemporal tracking algorithm (Uritsky et al. 2007, 2010a) which treats photospheric or coronal features staying for more than one image sampling interval above a specified detection threshold as subvolumes in the three-dimensional space-time. The time history of each feature is represented by

spatially and temporally connected sets of image pixels.

The idea of the threshold-based spatiotemporal feature tracking has first been implemented in the context of solar magnetograms by Berger & Title (1996); Berger et al. (1998). The object tracking method used in their study was based on measuring the centroid locations of the most compact and intense magnetic features. Here we invoke a different approach which does not rely on the centroid location as a guiding center for feature tracking. Time-evolving magnetic concentrations are treated as true 3-dimensional objects, which makes it possible to study a more general class of magnetic and emission structures whose positions cannot be adequately described by a centroid. Compared to more recent works, our algorithmic solution reverses the usual order of feature tracking steps (feature segmentation within an individual image followed by cross-frame feature identification within an image set, see e.g. DeForest et al. (2007)). Instead, we start with detecting temporal traces of features in individual solar locations, and then consider their spatial adjacency. We found this algorithmic solution to be remarkably fast and memory-efficient, with the size of the output data array being typically at least by two order of magnitudes smaller compared to the original data. A more complete description of the developed algorithm and its numerical validation on high-Reynolds number magnetohydrodynamic turbulence can be found in (Uritsky et al. 2010b).

Both data sets (MDI and EUVI) are characterized by broad distributions of pixel values (Fig. 3), encompassing more than three orders of magnitude for the magnetic field and about two orders of magnitude for the EUVI flux. In an attempt to make the event detection consistent with the dynamic range of each data sets, we set the detection thresholds to percentile levels $p = 95.0, 97.0, 99.0, 99.5\%$ defining the percentage of image pixels above a threshold. The dimensional thresholds corresponding to the chosen set of percentiles in MDI and EUVI data are shown with vertical lines in the Fig. 3. Table 1 shows the thresholds values and the amounts of detected events corresponding to these thresholds.

By applying the described method, we identified all distinct path-connected sets (Sherbrooke et al.

1996) of spatiotemporal coordinates satisfying the threshold condition and representing separate events. Fig. 4 provides an illustration of some of the events detected in the conjugate MDI and EUVI data sets at $p = 95\%$.

Each solar event was characterized by the lifetime T (time interval between the last and the first image frames involving the event), the peak instantaneous area A covered by the event at any given time, the total area S of the entire spatial region involved in the event during T , the dimension L_{lat} (L_{lon}) of this region in latitudinal (longitudinal) direction used to estimate the linear scale $L = (L_{lat}^2 + L_{lon}^2)^{1/2}$ of the event, the 3-dimensional spatiotemporal volume V of the event obtained by summing all district combinations of spatial and temporal coordinates attributed to the event, and the integrated intensity E of the event evaluated by integrating the measured parameter (either LOS magnetic flux or EUVI emission flux) over V .

To quantify multiscale behavior of the detected events, the following scaling model has been applied:

$$f(X) \propto X^{-\tau_x} \quad (1)$$

$$X \propto L^{D_x} \quad (2)$$

Here, $X \in \{T, L, A, S, V, E\}$ is one of the estimated event parameters, $f(X)$ is its probability distribution, τ_x is the so-called distribution exponent of X describing the log-log decay of $f(X)$, and D_x is the geometric exponent characterizing the power-law scaling of the studied parameter with respect to the linear size L in terms of the conditional expectation value $E[X|L] \sim L^{D_x}$ (Biham et al. 2001). The scaling ansatz described by eq. (1)-(2) is widely used in the theory of nonequilibrium critical phenomena, in particular, for describing processes of critical percolation (Munoz et al. 1999), fractal surface growth (Barabási & Stanley 1995), and self-organized criticality (Bak et al. 1987, 1988).

Throughout this paper, we use the “hat” symbol to distinguish coronal scaling exponents \hat{D}_x and $\hat{\tau}_x$ from their photospheric counterparts D_x and τ_x .

Fig. 5 shows the statistical dependence of magnetic and emission event parameters (lifetime T , peak area A , total area S , spatiotemporal volume

V and integrated flux E) on the linear size L of the event obtained for the 95% thresholds. Overplotted with the scatterplots are averaged regression dependences (solid lines with error bars) computed by coarse-graining the data using exponentially increasing L -bins.

The scatterplots in Fig. 5 show a power-law increase of the studied parameters with L . The power law dependence is distorted at the smallest L scales due to the insufficient spatial resolution of the data, as well as at the largest scales which are typically affected by finite-size effects and/or poor statistics (Robinson 1994; Uritsky et al. 2006). To obtain robust statistical measures of multiscale behavior, it is important to focus on the intermediate range of L scales which is free of such distortions, and to make the ranges of all other parameters consistent with the selected L range. Based on the shape of $A(L)$ dependence, we set the smallest and the largest linear scales to respectively $L_1=3$ Mm and $L_2=12$ Mm, with $L_1 < L < L_2$. We found that the upper scale limit L_2 can be increased up to at least 15 Mm without affecting the main results of this study. Reducing the lower limit L_1 leads to less accurate estimates caused by the inclusion of small-scale events which are not properly resolved. The same L -scale limits were applied to MDI and EUVI data sets to ensure consistent statistical estimates.

The geometric exponents D_x and \hat{D}_x describing respectively photospheric and coronal events were determined based on power-law regression fits to the original (non coarse-grained) data inside the interval $L \in (L_1, L_2)$. The tilted dashed lines in each of the panels of Fig. 5 show the log-log slopes of the regression fits. The slopes are supplemented by the average values and standard errors of the evaluated geometric exponents. The obtained regression models were used to calculate scaling ranges of all other parameters; these ranges were subsequently used to measure the distribution exponents:

$$X \in (a_x L_1^{D_x}, a_x L_2^{D_x}) \quad \text{for the photosphere} \quad (3)$$

$$X \in (\hat{a}_x L_1^{\hat{D}_x}, \hat{a}_x L_2^{\hat{D}_x}) \quad \text{for the corona}, \quad (4)$$

where a_x and \hat{a}_x are the regression coefficients evaluated for the two solar regions and L_1 (L_2) are the lower (upper) limits of the studied L range as explained above. The studied ranges of L scales

are shown in each of the Fig. 5 panels by vertical dot-dashed lines, with the matching intervals of scales of conjugate parameters computed based on eq. (3) shown by horizontal lines.

Probability distributions of MDI and EUVI events for all four percentile thresholds are presented in Fig. 6. The ranges of scales used to evaluate power law slopes of each histogram were calculated using eq. 3. These ranges are marked by vertical dash-dotted lines and correspond to the horizontal lines in the previous figure. It can be seen that the distributions decay as approximate power laws, consistent with earlier observations of power law statistics in solar photosphere and corona (Crosby et al. 1993; Abramenko et al. 2002; Aschwanden & Parnell 2002; Aschwanden 2011; Crosby 2011; Aschwanden 2013).

The broad-band power-law behavior of MDI distributions suggests that the dynamics of the LOS photospheric magnetic field is an inherently multiscale process (Uritsky & Davila 2012). Our threshold-based definition of magnetic events is clearly not limited to the injection of new magnetic bipoles into the photosphere and their subsequent submergence into the convection zone. In essence, we deal with an apparent dynamics associated with crossings of the percentile detection threshold by the local magnetic field. The resulting sets of events likely contain a combination of truly emerging and submerging magnetic bipoles as well as magnetic flux coalescence, fragmentation, cancellation, injection of upwardly propagating Alfvénic wave packets (De Pontieu et al. 2007), and other effects leading to spatiotemporal variability of the photospheric field. As we demonstrate below, the dominating factor leading to the multiscale statistics of this complex set of events is random footpoint shuffling driven by turbulent convective flows (see e.g. Lamb et al. (2008); Chaouche et al. (2011); Crouch et al. (2007); Simon et al. (1995, 2001)).

The values of EUVI distribution exponents, as well as SOHO EIT exponents reported in our earlier study (Uritsky et al. 2007), suggest that solar corona operates in a highly intermittent turbulent state consistent with models of self-organized criticality (Bak et al. 1987; Lu & Hamilton 1991). It should be noted, however, that the exponents reported here are obtained using spatiotemporal definition of events which is conceptually much

closer to measuring avalanches in numerical simulations of self-organized criticality than most of the definitions used in previous works on flare statistics conducted by other authors - except for a few case studies (Berghmans et al. 1998; Berghmans & Clette 1999) focusing on specific coronal conditions. The energy distribution exponent $\hat{\tau}_E < 2$ indicates that the coronal dynamics is likely to be dominated by large events as opposed to Parkers scenario of nanoflare heating (Parker 1988). Coronal energy scaling exponents below the value 2 have been obtained in many previous studies including those based on spatiotemporal detection of coronal brightenings and their spatial detection with subsequent integration of the emission fluxes over fixed time interval (e.g. Aschwanden et al. 2000a,b). As we argue below, such exponent values suggest that small heating events are not frequent enough to account for the bulk coronal heating. The difficulty with ascribing this role to the large events is that they are unable to supply the required energy loss rates of $10^5 - 10^7$ erg/cm²/s (see e.g. Athay 1966).

The exponent $\hat{\tau}_T$ is consistent with previous analyses of threshold-dependent inter-occurrence times of x-ray bursts measured over the whole Sun (Baiesi et al. 2006), as would be expected if total emission were a sum over individual avalanches (Corral & Paczuski 1999). We also note that this and other EUVI distribution exponents are in an approximate agreement with the results of forced MHD simulation of turbulent coronal heating (Dmitruk & Gomez 1997).

Table 2 provides a summary of geometric and distribution scaling exponents in the photosphere and corona for all four detection thresholds. In addition, the table contains the auxiliary scaling indices $\Delta_x \equiv D_x(\tau_x - 1)$ and $\hat{\Delta}_x \equiv \hat{D}_x(\hat{\tau}_x - 1)$. For a given threshold and data type, these indices are expected to be independent of X (constant across all event parameters) due to the probability conservation implying $f(X)dX \sim f(L)dL$ for any X . A deviation of Δ_x ($\hat{\Delta}_x$) from the values $D_L(\tau_L - 1) \equiv \tau_L - 1$ ($\hat{D}_L(\hat{\tau}_L - 1) \equiv \hat{\tau}_L - 1$) by more than $\sim 10\%$ signals an insufficient statistics and/or an inadequate scaling model. Such cases are marked by asterisk in Table 2.

Table 2 shows that the probability distributions of MDI and EUVI events corresponding to the same percentile level are characterized by signif-

icantly different power law slopes yielding distinct τ_x exponents. In particular, the τ_x values characterizing photospheric events obtained at the 95% detection threshold are substantially higher compared to the corresponding $\hat{\tau}_x$ values describing EUVI events obtained at the same threshold.

We found that the difference in the scaling behavior of the two solar regions originates in the difference of the intermittency level of events detected at the same percentile thresholds. As Table 1 indicates, for any given percentile threshold, the number of MDI events is considerably larger compared to the number of EUVI events. For the lowest applied threshold, the discrepancy reaches an order of magnitude. This suggests that for the same p , the magnetic events are much more intermittent than the coronal events. Applying a smaller threshold to a spiky MDI magnetogram results in much more threshold crossings, and hence more time-integrated events. Due to a much smoother spatial pattern of the coronal emission field, the same procedure leads to a less significant increase in the number of the detected coronal events.

Physically, it is clear that comparing populations of MDI and EUVI events obtained at the same detection threshold is not justified because such events represent different types of conditions characterized by incomparable occurrence rates. Indeed, there is no reason to expect that a frequently occurring photospheric condition is described by the same statistics as a rarely observed class of coronal events. To make the comparison of the photospheric and coronal events more consistent, one needs to make sure that the detected populations of events have approximately the same size - in other words, they are described by *the same degree of intermittency*. To attain this goal, one needs to set the magnetic threshold to a higher percentile level compared to the emission threshold.

Based on the population sizes provided in Table 1, the 99.0% (99.5%) magnetic events have approximately the same degree of intermittency as the 95.0% (97.0%) heating events. Pairwise comparison of these sets of events (99.0% MDI vs. 95.0% EUVI, 99.5% vs. 97.0%) shows that they are described by drastically different geometric exponents but surprisingly close distribution exponents, especially those for the time-integrated

parameters S , V and E (see Table 2). As we show in Section 3.3, the distinct values of the linear scale distribution exponent in the photosphere and corona are consistent with the geometries of the intermittent events in the two system.

Fig. 7 presents a direct comparison of the probability distributions of MDI and EUVI events over the three measures S , V and E involving spatiotemporal integration. The distributions are built using the pairs of percentile thresholds yielding consistent population sizes. To construct the distributions, we consider only the events whose linear sizes lie within the scaling interval of interest (L_1, L_2). No other transformations besides the standard probability density normalization were applied to the histograms. The obtained MDI and EUVI distributions are remarkably similar in shape and are described by fairly close probability values. Within the statistical accuracy, they effectively coincide for both combinations of thresholds. The plotted spatiotemporal measures of coronal emission events obey the same occurrence probabilities as the corresponding measures of photospheric magnetic events.

The similarity of coronal and photospheric distribution exponents is also evident from Fig. 8 which shows time evolution of the exponents evaluated within a 90-minute moving window. The wide error bars reflecting the lack of the sufficient number of events prevent us from drawing solid conclusions regarding the observed trends, although it seems plausible that the probabilistic laws describing the two data sets are dynamically coupled.

These observations are in line with the analysis of unstable magnetic discontinuities identified based on linear force-free extrapolation of photospheric field (Vlahos & Georgoulis 2004). Using this technique, Vlahos & Georgoulis (2004) have found a large number of magnetic discontinuities whose free magnetic energies and volumes obey power-law distribution functions. The log-log indices of the distributions were found to be in agreement with the indices describing the occurrence frequencies of solar flare energies reported in the literature. Based on this comparison, Vlahos & Georgoulis (2004) speculated that the statistics of flares may result from a preexisting free energy fragmentation in the solar corona. Solar flares occur in unstable coronal volumes as-

sociated with discontinuities in the coronal magnetic field. It is expected that not every single unstable magnetic volume generates a flaring event, but most of the flares do occur in such pre-existing unstable volumes containing strong nonpotential magnetic field.

Our statistical analysis based on conjugate sets of coronal and photospheric observations provides an opportunity for a more direct test for this coupling scenario. Taken at face value, the statistics shown in Fig. 7 support the picture in which the coronal emission events are generated in a random subset of unstable magnetic volumes created by the photospheric motion. The quantitative analysis of scaling relations between coronal and photospheric power-law exponents presented in Section 3.3 below lead us to the same conclusion. At the same time, our results do not rule out a possibility of a different underlying physics involving multiscale pulses of upwardly propagating Alfvénic waves (Suzuki & Inutsuka 2006; Ulrich 1996; Fujimura & Tsuneta 2009) as discussed in section 3.4.

3. Discussion

In this section, we look closer at the spatiotemporal geometry of magnetic and emission events in an attempt to derive scaling relations between the observed scaling exponents. The analysis is validated using the averaged scaling exponents describing MDI events detected at $p = 99\%$ and $p = 99.5\%$ thresholds, as compared to the averaged exponents of EUVI events obtained at $p = 95\%$ and $p = 97\%$. As mentioned earlier in the text, the sets of events corresponding to these thresholds are described by comparable levels of intermittency resulting in consistent population sizes. The exponent values used for the validation and are provided in Table 3. While the numerical values of the exponents vary with the detection threshold (Table 2), the relations between the exponents discussed in this section are expected to be insensitive to the threshold as long as the MDI and EUVI events have comparable population sizes. As before, we use the hat symbol ($\hat{\cdot}$) to distinguish coronal parameters from their photospheric counterparts.

3.1. Scaling of the magnetic events

According to the accepted scaling model (2), the scaling of linear size of the event with the event duration is governed by the geometric exponent D_T :

$$L \propto T^{1/D_T} = T^H, \quad (5)$$

Since $D_T \approx 2.18$ (Table 3) the diffusive exponent $H \approx 0.46$ is close to the value $1/2$. This means that the linear size of the perturbation scales approximately as a square root of the elapsed time. Such scaling is characteristic of the classical (as opposed to fractional) random walk (Mandelbrot & VanNess 1968) which can be a manifestation of random footpoint shifting of the photospheric field (see e.g. Simon et al. (1995, 2001); Rast (2003); Crouch et al. (2007)). The idea of the random footpoint shuffling has been recently used for constructing a statistical fractal-diffusive self-organized criticality model (FD-SOC) (Aschwanden 2012a,b). The standard FD-SOC model (Aschwanden 2012b) with $H = 1/2$ predicts the geometric and distribution exponents which are fairly close to the exponents of the MDI events reported in Table 3.

Assuming that the average magnitude of the horizontal convective flow associated with the shuffling is independent of L within the studied range of spatial scales, we get a simplified picture (Fig. 9(a)) in which the swept area of the event scales approximately as $S \propto \ell T$, where $\ell \sim A^{1/2}$ is a measure of the instantaneous linear scale of the event. Therefore we have $S \propto A^{1/2} T \propto L^{\frac{D_A}{2} + D_T}$ which, taking into account $S \propto L^{D_S}$, yields

$$D_S = \frac{D_A}{2} + D_T. \quad (6)$$

By plugging in the measured values of D_A and D_T we get $D_S \approx 2.88$. The direct evaluation of D_S based on the $S(L)$ regression leads to $D_S = 2.78 \pm 0.11$ showing that the relation (6) holds with a reasonable statistical accuracy.

The exponent D_V describing the scaling of spatiotemporal volume V of magnetic events can be also derived in frames of the random shuffling model implying that $V \sim A T$ (since the cross-section area A is orthogonal to the time axis, see Fig. 9(a)). Making use of $A \propto L^{D_A}$ and $T \propto T^{D_T}$ we get

$$D_V = D_A + D_T. \quad (7)$$

The relation (7) predicts $D_V \approx 3.57$ which agrees with the observed value $D_V = 3.43 \pm 0.12$.

It is important to clarify that the equation (6) is derived assuming that the instantaneous shape of magnetic elements is purely 2-dimensional. While this assumption is certainly not justified for high-resolution magnetograms featuring irregular magnetic geometry (Cadavid et al. 1994), it seems to be acceptable for describing SOHO MDI structures covering up to 10 Mm^2 at a time (the largest A consistent with the chosen L range, see Fig. 5) since such structures are too small to display identifiable fractal boundaries at the available resolution.

The dependence of the instantaneous linear size ℓ of magnetic elements on lifetime T reflects the dynamic behavior of the underlying physical processes acting at small spatial scales, such as e.g. magnetic flux coalescence, fragmentation, emergence and submergence (Lamb et al. 2008; Chaouche et al. 2011; Crouch et al. 2007; Simon et al. 1995, 2001; Welsch 2006). Even though these processes are not fully resolved in the studied data, their effective contribution can be evaluated based on the temporal scaling of magnetic element sizes as expressed by the measured geometric exponents. By combining $\ell \propto A^{1/2}$, $A \propto L^{D_A}$, and $L \propto T^{1/D_T}$ we obtain

$$\ell \propto T^{H_1}, \quad H_1 = \frac{D_A}{2D_T}. \quad (8)$$

Here, the diffusion index H_1 characterizes a small-scale transport of the photospheric magnetic field. Substituting $D_A \approx 1.39$ and $D_T \approx 2.18$ we get $H_1 \approx 0.32$. The obtained index shows that the small-scale magnetic field convection is strongly subdiffusive (Bouchaud & Georges 1990; Isichenko 1992), meaning that the size of the magnetic elements varies with time significantly slower than it would be expected for a regular diffusion described by a classical Brownian walk defined by $H_1 = 1/2$ (linear displacement proportional to the square root of the elapsed time). A subdiffusive transport usually takes place when the studied system contains spatial subdomains where the transported quantity becomes partially “trapped” (Metzler & Klafter 2000). In solar photosphere, such trapping can be due to the small-scale turbulence accompanying the granulation process (Espagnet et al. 1993) which is closely related to

the surface dynamo problem (Vögler & Schüssler 2007). According to Kolmogorov’s refined similarity hypothesis, the third moment of the distribution function of correlated velocity increments Δu observed at the characteristic distance ℓ scales as ℓ^{3H_1} (Stolovitzky & Sreenivasan 1994). Comparing this expression with Kolmogorov’s exact relation for inertial range turbulence (Monin & Yaglom 1975; Biskamp 2003) $\langle \Delta u(\ell)^3 \rangle = -\frac{4}{5} \langle \epsilon \rangle \ell$ (ϵ being the dissipation rate per unit mass) one gets $H_1 = 1/3$. This prediction is fairly close to the H_1 -value obtained for the photosphere in our study showing that that the range of sizes of magnetic elements addressed by this analysis ($\ell \equiv A^{1/2} \sim 2-4$ Mm, see Fig. 5) is likely to fall into the inertial range of the granulation-driven turbulence (Espagnet et al. 1993), and if so, the photospheric turbulence is locally isotropic.

3.2. Scaling of the emission events

In contrast to the photospheric events evolving approximately as $L \propto T^{1/2}$, temporal dependence of linear sizes of coronal events is strongly superdiffusive as revealed by $\hat{H} = 1/\hat{D}_T \approx 0.74$. The small-scale coronal diffusive exponent $\hat{H}_1 = \hat{D}_A/(2\hat{D}_T) \approx 0.59$ is also larger than the classical diffusion value. Superdiffusive behavior is known to arise in strongly nonlinear media containing spatially distributed regions in which the diffusive transport is anomalously fast (Metzler & Klafter 2000). Compared to the classical random walk with temporally uncorrelated increments, the superdiffusive walk, such as the one modeled by fractional Brownian motion (Mandelbrot & VanNess 1968), features significant positive correlations across all time scales involved in the process (Turcotte 1989; Feder 1988). The fact that $\hat{H} \neq \hat{H}_1$ suggests that the dynamics of coronal emission regions is a sum of two types of motion – a superdiffusive expansion of the event area and a displacement of the center of the event over a comparable distance (Fig. 9(b)).

The expansive superdiffusive growth of emission regions could be a manifestation of energy avalanches developing in the corona (see e.g. Crosby et al. (1993); Crosby (2011); Charbonneau et al. (2001); Aschwanden et al. (2000b); Aschwanden & Parnell (2002); Morales & Charbonneau (2008); Uritsky et al. (2007)). It has been suggested that the non-

potential magnetic field configurations existing in the corona release their free energy through a chain interaction of multiple spatially localized instabilities such as those associated with nanoflare heating (Parker 1988; Klimchuk 2006; Viall & Klimchuk 2011). The perturbation proceeds explosively by involving a growing number of unstable plasma regions, similarly to the interaction of rolling grains of sand leading to a sand pile avalanche (Bak et al. 1987, 1988). This scenario, known as self-organized criticality (SOC), has been extensively studied in the context of solar flares, starting from the pioneering work of Lu & Hamilton (1991) and followed by a variety of more recent numerical simulations (see Charbonneau et al. (2001) for a brief review). It is important to note that coronal energy avalanches may or may not be topologically compact. In the latter case, the super-diffusivity of solar corona can be a manifestation of multiple dissipation regions appearing in response to the same initial trigger (Török et al. 2011). The ensemble-based behavior of these regions would involve spatial jumps (such as those modeled by Lévy flights) associated with the appearance of new centers of activity, leading naturally to a superdiffusive \hat{H} value. The evolution of individual regions could follow a different scaling law and be subdiffusive during the impulsive phase of flares (Aschwanden 2012a).

Despite their major success in explaining scale-free cooperative phenomena, most of the SOC models are not solvable analytically (Jensen 1998) making it difficult to obtain closed-form relations characterizing observed statistical scaling laws. The first-principle analysis of such models is often an intractable task due to the involvement of higher-order statistical moments (Vespignani & Zapperi 1998; Sethna et al. 2001) requiring full dynamic renormalization group treatment (Chang 1992). However, this theoretical complication could be of little importance for the solar activity since its dynamics is not a pure SOC but combines both driven and self-organized components.

If the behavior of solar corona was fully analogous to SOC models, the spatial distribution of free magnetic energy in the corona would have to be solely formed by previous flaring events. However, coronal dynamics is fundamentally dif-

ferent. Although local triggers of coronal instabilities are largely unpredictable (Aschwanden 2011, 2013), spatial distribution of free magnetic energy supplied by the photosphere is far from random. For this reason, solar corona is a driven rather than a fully self-organized avalanching system. The present study confirms this interpretation by showing that solar photosphere places constraints on the occurrence probability of coronal events of different sizes.

As the next step, we look further into the growth and decay dynamics of coronal emission events as characterized by geometric and distribution exponents. Avalanching dynamics can be seen as a special case of spreading dynamics in active nonlinear media with spatially distributed energy sources and sinks (Vespignani & Zapperi 1998; Munoz et al. 1999). Spreading experiments provide the most accurate determination of the critical point of systems with multiple absorbing states (Grassberger & Delatorre 1979) such as avalanching systems at self-organized criticality (Vespignani et al. 2000). A small perturbation representing an initial instability is created at the origin of an otherwise absorbing configuration, leading to a spread of activity. At the critical point associated with power-law distributions of avalanche sizes (Bak et al. 1987; Robinson 1994; Sethna et al. 2001), the mean-squared deviation from the origin R^2 , the survival probability P , and the number N of unstable sites scale with time t as $R^2(t) \propto t^{\hat{z}}$, $P(t) \propto t^{-\hat{\delta}}$, and $N(t) \propto t^{\hat{\eta}}$ where \hat{z} , $\hat{\delta}$ and $\hat{\eta}$ are the spreading exponents describing the growth and decay of energy avalanches. In our measurements, P has the meaning of the cumulative distribution of avalanche lifetimes: $P(t) = \int_0^t f(T) dT \propto T^{-\hat{\tau}_T+1}$ and hence $\hat{\delta} = \hat{\tau}_T - 1$ (Uritsky et al. 2007; Morales & Charbonneau 2008).

The number of individual unstable events (toppling events in sandpile simulations (Bak et al. 1987), nanoflares in the Parker's heating scenario (Charbonneau et al. 2001)) associated with an avalanche with a lifetime T scales as $\propto T^{1+\hat{\eta}+\hat{\delta}}$ (Munoz et al. 1999; Uritsky et al. 2007; Morales & Charbonneau 2008). Approximating this number by the integrated emission flux E we obtain $E \propto T^{1+\hat{\eta}+\hat{\delta}} = L^{\hat{D}_T(1+\hat{\eta}+\hat{\delta})} \propto L^{\hat{D}_E}$ which

yields

$$1 + \hat{\eta} + \hat{\delta} = \frac{\hat{D}_E}{\hat{D}_T}. \quad (9)$$

Munoz et al. (1999) have argued that the relations between the spreading and the distribution exponents depend upon the universality class of the avalanching system. Here we accept their interpretation in terms of the directed and dynamical percolation classes governed by the well-known relation $\hat{z}d/2 = \hat{\eta} + 2\hat{\delta}$ (see Munoz et al. (1999) and references therein) which in our case can be rewritten as

$$\hat{z}d/2 = \frac{\hat{D}_E}{\hat{D}_T} + \hat{\tau}_T - 2 \quad (10)$$

where d is the Euclidean dimension of coronal avalanches. Also, from the definition of the \hat{z} exponent it follows that

$$\hat{z} = \frac{\hat{D}_S}{\hat{D}_T}. \quad (11)$$

where we took into account that $R^2 \sim S$ and $t \sim T \propto L^{\hat{D}_T}$. By solving eqs. (10-11) for d and substituting the measured coronal exponent values we find that $d \approx 3$, with the value $\hat{z} \approx 1.47$ predicted by eq.(11) being in an agreement with the behavior of three-dimensional dynamical percolation (Munoz et al. 1999).

These estimates suggest that coronal dissipation takes place in 3-dimensional plasma volumes. Elementary instabilities associated with individual nanoflares can, in principle, have a different dimensionality, for instance $d = 2$ for reconnecting current sheets. However, our estimates show that the interaction network controlling growth and decay of coronal emission regions is likely to be embedded in a 3-dimensional space, and is also space-filling (Mandelbrot 1977).

In coronal heating studies, the value $d = 3$ is often taken for granted (Aschwanden et al. 2000b; Parnell & Jupp 2000; Krucker & Benz 1998; Mitra-Kraev & Benz 2001). The analysis conducted here justifies this choice speaking in favor of a three-dimensional emitting plasma volume, as opposed to more complex geometries described by $d < 3$ as predicted by some statistical-physical models of solar flares (McIntosh & Charbonneau 2001).

The derived three-dimensional geometry of energy avalanches in the corona is consistent with other scaling exponents. The swept area S of each event can be considered as a two-dimensional projection of a d -dimensional shape. The dimension d_p of the projection (approximated in our case by \hat{D}_S by the definition of fractal dimension (e.g., Turcotte 1997)) is related to the dimension of the projected object as $d_p = d - 1$ (Mandelbrot 1982). For $d = 3$, the relation predicts $\hat{D}_S = 2$ which matches exactly the measured value 2.00 ± 0.03 of this coronal exponent. Also, assuming (as before) that the integrated emission flux E is proportional to the number of the unstable coronal sites constituting an avalanche, we expect $E \propto L^{\hat{D}_E}$ with $\hat{D}_E = 3$, which is in an agreement the empirical result $\hat{D}_E = 3.06 \pm 0.05$.

3.3. Stochastic coupling relations

Our observations indicate that the MDI and EUVI events are described by rather similar probability distributions of S , V and E parameters but, at the same time, by considerably different geometric scaling laws yielding distinct sets of D_x and \hat{D}_x exponents (see Table 3). This section aims to resolve the apparent controversy by connecting the two groups of exponents in through a set of stochastic scaling relations between the photosphere and corona. In section 3.4, these relations are used to provide a new insight into the physics of the underlying photosphere - corona coupling.

As a starting point, consider the subsets of coronal and photospheric events characterized by the same probability of occurrence. Since the probability distributions of the swept areas of coronal and photospheric events coincide, this requirement is equivalent to $S = \hat{S}$ (coronal measures are labeled by the hat symbol).

Eq. (2) suggests that the linear scales describing the considered events are related as $L^{D_S} \propto \hat{L}^{\hat{D}_S}$ yielding

$$\hat{L} \propto L^\alpha, \quad \alpha = \frac{D_S}{\hat{D}_S} \approx 1.39. \quad (12)$$

meaning that the apparent linear sizes of the coronal events are larger for the same swept area. The new scaling index α defined by the ratio of the measured values of D_S and \hat{D}_S exponents couples the linear scales of equally probable coronal and

photospheric events. The fact that $\alpha > 1$ means that the characteristic length of coronal emission regions grows faster with the swept area compared to the length scale of photospheric events. The difference in the scaling behavior of the two systems expressed by α should hold under any linear transformation maintaining $S \propto \hat{S}$. The power-law relation (12) between probabilistically equivalent photospheric and coronal scales accounts for *nonlinear* corrections to such geometric transformations associated with a physical interaction between the two system.

Next, consider the lifetimes of the selected subsets of events described by $S = \hat{S}$. Since $T \propto L^{D_T}$ and $\hat{T} \propto \hat{L}^{\hat{D}_T}$, we have a similar scaling law for the lifetimes of the coronal and photospheric events, with a differing value of the power-law index:

$$\hat{T} \propto T^\beta, \quad \beta = \frac{D_S \hat{D}_T}{D_T \hat{D}_S} \approx 0.87. \quad (13)$$

The obtained value of temporal coupling index β indicates that the duration of coronal emission events increases slower with the event area compared to the duration of photospheric events.

The relations (12)-(13) suggest that the observed similarity of $f(S)$ and $f(\hat{S})$ distributions is achieved through a nontrivial rescaling of spatiotemporal dimensions of solar events, with the coronal emission events lasting a shorter time but propagating over larger distance compared to the photospheric shuffling events described by the same occurrence rate.

Our goal now is to derive coupling relations expressing coronal geometric and distribution exponents as functions of the photospheric exponents and the empirical indices α and β .

By definition, the linear scale geometric exponent is identical to unity in both data sets, and so

$$\hat{D}_L = D_L (\equiv 1). \quad (14)$$

The exponent \hat{D}_S is already connected with D_S through the empirical scaling index α (12). It can be also linked to other photospheric indices. By combining the swept area expression for the photosphere (6) with the coupling relation (12) we obtain $S \propto (\hat{L}^{-\alpha})^{\frac{D_A}{2} + D_T}$. After equating S with $\hat{S} \propto \hat{L}^{\hat{D}_S}$, this equation provides an alternative

form for the coronal exponent \hat{D}_S :

$$\hat{D}_S = \frac{D_S}{\alpha} = \frac{D_A + 2D_T}{2\alpha}. \quad (15)$$

This relation predicts $\hat{D}_S \approx 2.0$ which coincides with the measured value for this exponent (2.00 ± 0.03).

Similarly, by plugging (12) and (13) into the scaling ansatz $\hat{T} \propto \hat{L}^{\hat{D}_T}$ and substituting L^{D_T} for T we obtain

$$\hat{D}_T = \frac{\beta}{\alpha} D_T \quad (16)$$

which yields the correct result $\hat{D}_T \approx 1.36$ as expected from the definition of α and β .

For deriving the exponent \hat{D}_A describing the geometric scaling of the peak area \hat{A} of coronal emission events one should take into account fractal (non-integer) dimension d_F of the emission regions defined by $\hat{A} \propto \hat{\ell}^{d_F}$. In frames of our model (Fig. 9(b)) the area \hat{S} covered by an emission event results from the combination of the avalanche-like expansion of the unstable region and the systematic displacement of its centroid. The characteristic linear scales of these effects are given respectively by $\hat{\ell}$ and \hat{L} from which it follows that $\hat{S} \propto \hat{L}\hat{\ell} = \hat{L}^{1+\frac{\hat{D}_A}{d_F}}$ and therefore

$$d_F = \frac{\hat{D}_A}{\hat{D}_S - 1}. \quad (17)$$

The obtained relation allows us to evaluate the fractal dimension $d_F \approx 1.6$ without performing direct scaling analysis which would likely to be inaccurate due to the smallness of $\hat{\ell}$ and limited spatial resolution of EUVI images. Using (17) along with the coupling relation for \hat{D}_S (15) we get

$$\hat{D}_A = \hat{d}_F \left(\frac{D_S}{\alpha} - 1 \right). \quad (18)$$

By the definition of α and d_F , the obtained expression matches the measured value $\hat{D}_A = 1.60 \pm 0.02$.

The exponent \hat{D}_V can be related to D_V by making use of the similarity of probability distributions of spatiotemporal volumes of coronal and photospheric events (Fig. 7), by analogy with the analysis of the exponent \hat{D}_S presented above. For a given occurrence rate, $\hat{V} = V$ and hence $\hat{L}^{\hat{D}_V} \propto L^{D_V}$, which after applying the spatial

rescaling (12) provides

$$\hat{D}_V = \frac{D_V}{\alpha}. \quad (19)$$

Comparing (15) and (19) leads to the identity $(\hat{D}_S D_V)/(\hat{D}_V D_S) = 1$ which is approximately fulfilled (substitution of the measured exponents yields ~ 0.95).

Expressing the emission flux exponent \hat{D}_E via the photospheric exponents presents a critically important (albeit somewhat more challenging) task because this exponent, along with the distribution exponent $\hat{\tau}_E$, can be used for forecasting coronal emission level. Using the relations (10) and (11) for the coronal spreading exponent \hat{z} along with the coupling relations (15) and (16), after some algebra we arrive at

$$\hat{D}_E = \frac{\beta D_T}{\alpha} \left(\frac{d D_S}{2\beta D_T} - \hat{\tau}_T \right) \quad (20)$$

Note that this is an intermediate result because it depends on the coronal exponent $\hat{\tau}_T$ which is yet to be related to derived.

The general form for any distribution exponent $\hat{\tau}_x$ follows directly from the probability conservation condition $f(\hat{X})d\hat{X} = f(X)dX$ where \hat{X} and X stand for the same type of measures in the corona and photosphere. Assuming a power-law scaling relation $\hat{X} = X^{\gamma_x}$ between the coronal and photospheric measures and applying the power-law scaling model (1) we get $f(\hat{X})d\hat{X} \propto X^{-\gamma_x \hat{\tau}_x} X^{\gamma_x - 1} dX \propto X^{-\tau_x} dX$ and consequently

$$\hat{\tau}_x = \frac{\tau_x - 1}{\gamma_x} + 1, \quad \gamma_x = \frac{\hat{D}_x}{D_x} \alpha \quad (21)$$

where the expression for γ_x follows from $\hat{X} \propto \hat{L}^{\hat{D}_x} \sim (L^\alpha)^{\hat{D}_x} \sim ((X^{1/D_x})^\alpha)^{\hat{D}_x} \sim X^{\frac{\hat{D}_x}{D_x} \alpha}$. By using the expressions for coronal geometric exponents derived above, one can easily calculate the corresponding value of γ_x and on this basis $\hat{\tau}_x$. In particular, for the linear size distribution exponent we have $\gamma_L = \alpha$ (since $\hat{D}_L = D_L \equiv 1$) and

$$\hat{\tau}_L = \frac{\tau_L - 1}{\alpha} + 1. \quad (22)$$

In its turn, the lifetime distribution exponent can be derived in a similar fashion by taking into consideration eq.(16) which yields $\gamma_T = \beta$ and therefore

$$\hat{\tau}_T = \frac{\tau_T - 1}{\beta} + 1. \quad (23)$$

The relations (22) and (23) result in the estimates $\hat{\tau}_L \approx 2.55$ and $\hat{\tau}_T \approx 1.91$ which fall within statistical uncertainty of the measured values $\hat{\tau}_L = 2.57 \pm 0.13$ and $\hat{\tau}_T = 2.02 \pm 0.07$.

Finally, after the substitution of (23) into (20) we obtain the geometric exponent of the emission flux as a function of the photospheric scaling exponents and the empirical coupling indices α and β :

$$\hat{D}_E = \frac{dD_S/2 + (\beta - \tau_T + 1)D_T}{\alpha}. \quad (24)$$

For space-filling 3-dimensional emission regions ($d = 3$) the relation (24) predicts $\hat{D}_E \approx 3.12$ which is approximately consistent with the observed $\hat{D}_E = 3.06 \pm 0.03$.

The last column in Table 3 provides a summary of the coronal distribution exponents predicted using the scaling relations discussed in this section.

3.4. Energy considerations

The analysis of scaling relations presented so far reconciles the obtained results showing that the difference in the geometry of photospheric and coronal events is expected for physical reasons, and is consistent with the similarity of the statistics describing spatiotemporal event measures S , V and E . The derived scaling laws suggest a simple coupling scenario in which the footpoints of the coronal flux tubes undergo a quasi one-dimensional horizontal convective motion given by a vector sum of uncorrelated displacements (a random walk behavior) while the coronal emission events are three-dimensional, with the grow and decay dynamics being similar to that of SOC models. When integrated over space and time, the two groups of events exhibit indistinguishable distribution functions.

The physical agent that provides the most natural explanation for the observed probabilistic coupling between solar photosphere and corona is the nonpotential magnetic energy supplied by the photospheric shuffling.

The normal Poynting flux S_n of energy through the base of the corona in the ideal magnetohydrodynamic approximation can be written as

$$S_n = \frac{c}{4\pi} \mathbf{n} \cdot \left(-\frac{\mathbf{v} \times \mathbf{B}}{c} \times \mathbf{B} \right) \quad (25)$$

in which \mathbf{v} is the photospheric velocity and \mathbf{n} is

the unit normal vector (for simplicity the magnetic diffusivity is assumed to be negligible). A similar expression can be written for the potential magnetic energy flux; the difference between the two fluxes yields the flux of *free* magnetic energy into the corona (Welsch 2006):

$$S_n^{(F)} = \frac{1}{4\pi} \left(\mathbf{B}_h - \mathbf{B}_h^{(P)} \right) \cdot (v_n \mathbf{B}_h - \mathbf{v}_h B_n) \quad (26)$$

where the subscripts h (n) denote the horizontal (normal) components of the velocity and magnetic field vectors and $\mathbf{B}_h^{(P)}$ is the potential horizontal field. The studied FoV is close to the center of the solar disc where SOHO MDI flux counts provide a reasonable proxy to \mathbf{B}_n . The behavior of the horizontal velocity can be evaluated indirectly based on the tracks of the magnetic features as discussed in section 3.

Assuming that the difference between the total and the potential horizontal magnetic fields remains constant during each event and ignoring the contribution from the $v_n \mathbf{B}_h$ term which cannot be evaluated from the studied data, we find that on average,

$$S_n^{(F)} \propto \langle v_h \rangle \langle B_n \rangle \quad (27)$$

with $\langle v_h \rangle$ and $\langle B_n \rangle$ being the characteristic values of the horizontal flow velocity and the line of sight magnetic field, respectively. The sign of $S_n^{(F)}$ in eq. (27) is positive since we are not interested in the events producing a downwardly directed Poynting flux $S_n^{(F)} < 0$.

According to our statistical results, the dynamics of the photospheric footpoint shuffling is close to classical random walk with $H = 1/2$. This dynamics has been shown to be critically important for the generation of the upward Poynting flux, especially in strongly magnetized intergranular lanes experiencing horizontal vortex motions (Shelyag et al. 2012). The velocity field satisfying the $H = 1/2$ condition is described by a stable probability distribution with finite and constant first and second moments (Turcotte 1997). Based on this model, one can assume that $\langle v_h \rangle$ remains constant during each event and is not a function of its linear scale L (such a dependence would imply a super- or sub-diffusive behavior of the magnetic events which is not observed). The quantity $\langle B_n \rangle$ can be easily obtained based on the conducted scaling analysis. The spatiotemporal sum

of magnetic flux counts during the events scales as $\propto L^{D_E}$ while the spatiotemporal volume scales as $\propto L^{D_V}$. The ratio between these two quantities gives the required average field:

$$\langle B_n \rangle \propto L^{D_E - D_V} \quad (28)$$

The free magnetic energy W produced by any given shuffling event can be evaluated by integrating eq. (27) over the involved surface area and the event lifetime:

$$W \propto \langle v_h \rangle \langle B_n \rangle \int_T dt \int_{x,y \in a(t)} dx dy \quad (29)$$

in which $a(t)$ is the instantaneous area of the event at time t . It is easy to verify that the domain of the integration in eq. (29) is nothing but the swept area S of the event, according to our definition of this parameter. By making use of this fact and substituting (28) for the magnetic field we arrive at the geometric scaling law for the energy of the shuffling event:

$$W \propto L^{D_E - D_V + D_S}. \quad (30)$$

Substitution of the estimated values of the photospheric scaling exponents involved in this relation yields $W \propto L^{D_W}$ with $D_W \approx 3.15$. This estimate is in a decent agreement with the geometric exponent $\hat{D}_E = 3.04 \pm 0.03$ characterizing the power-law scaling of the coronal emission flux with L . Therefore, the shuffling energy and the coronal emission energy in the populations of coronal and photospheric events described by the same rate of occurrence are *directly proportional*. While the proportionality itself does not necessarily imply a causal link, it clearly speaks in favor of a photospheric input working as a driver of coronal dissipation.

The described coupling scenario is reminiscent of the famous Parker's scenario of nanoflare coronal heating. However, the similarity can be misleading for the following reasons. First, the physical scales of the coronal events included in our analysis is incomparably larger than the size of the nanoflares. This is because the detection threshold used to extract the events was tuned to a fairly high emission level which produced small apparent sizes but in fact ensured that most of the low intensity coronal brightenings were excluded from the statistics. Secondly, if we postulate that

the smaller events (unresolved by our technique) obey the same statistical laws as the observed events, the obtained value $\hat{\tau}_E \approx 1.5 < 2$ of the emission exponent predicts that the energy outputs from the small events (possibly including the nanoflares) is negligible compared to the contribution of large events since the ensemble averaged emission flux

$$\langle E \rangle = \int_{E_{min}}^{E_{max}} E f(E) dE \propto E^{2-\hat{\tau}_E} \Big|_{E_{min}}^{E_{max}} \sim (E_{max})^{0.5}. \quad (31)$$

is controlled by the largest flares. On the other hand, the ratio between the free magnetic energy of a given shuffling event (30) to the average total magnetic energy per unit area during the event increases with decreasing L :

$$\frac{\text{Free magnetic energy}}{\text{Total magnetic energy}} \propto \frac{W}{\int_V B_n^2 dv} \quad (32)$$

$$\propto \frac{L^{D_E - D_V + D_S}}{L^{2(D_E - D_V) + 3}} = \frac{L^{3.15}}{L^{3.74}} \sim L^{-0.84} \quad (33)$$

in which we used the energy scaling relation (30) for W , equation (28) for the average LOS magnetic field during the event, and have assumed a 3-dimensional coronal volume. The fact that the resulting power law exponent is negative indicates that the small-scale magnetic events are on average much more effective as free energy sources compared to the large events. The higher relative occurrence rate of the small shuffling events could make this dependence statistically quite important. However, the net free energy outcome from the small photospheric events is still smaller than that from the large events because the power-law exponent τ_W of the W distribution predicted by the probability conservation ($D_W(\tau_W - 1) = D_L(\tau_L - 1) \Rightarrow \tau_W \approx 1.7$) is, again, below the value 2.

An alternative line of interpretation of the observed energy scaling laws could involve multi-scale Alfvénic wave packets excited in the chromosphere and corona by the photospheric footpoint motions (e.g., Ofman et al. 1998; Ulrich 1996; Kudoh & Shibata 1999; Suzuki & Inutsuka 2006; De Pontieu et al. 2007; Fujimura & Tsuneta 2009; Ofman 2010). Perturbations in the photosphere are able to generate a broad spectrum of transverse waves with the statistical properties of the generating convective events. Once these

waves arrive at the corona they should result in dissipation events with similar statistics.

In the Wentzel-Kramers-Brillouin approximation, the energy flux of an Alfvén wave packet generated by a single shuffling event associated with the displacement velocity v_d is given by

$$S_n^{(A)} = \rho v_d^2 V_A \quad (34)$$

in which ρ is the ambient mass density and V_A is the local Alfvén speed. Assuming that the displacement velocity $v_d \approx \langle v_h \rangle$ is roughly constant (see the Brownian walk argument above) and the plasma is homogeneous, integration of (34) over the emitting area and time yields the Alfvén energy

$$W_A \propto \langle v_h \rangle^2 \langle B_n \rangle \int_T dt \int_{x,y \in a(t)} dx dy \quad (35)$$

Since $\langle B_n \rangle \sim E/V$ and the domain of the integration is defined the swept area S , we arrive at the scaling law

$$W_A \propto L^{D_E - D_V + D_S} \equiv L^{D_W} \quad (36)$$

which is identical to (30). Thus, the wave mechanism leads to the same geometric scaling of the energy input from the photosphere as the one based on the nonpotential MHD Poynting flux. Both mechanisms predict $D_W \approx \hat{D}_E$ and are in an agreement with the statistics of coronal energy dissipation presented in section 2. The wave mechanism is it more likely to play a role in the generation of short-living coronal events while the long-lasting events could be driven by slow convective shuffling. Understanding the detailed interplay between these effects in the context of the multiscale photosphere - corona coupling is an important task for future research.

4. Conclusions

The presented statistical results reveal a striking similarity in the behavior of coronal emission events (as measured by transient localized enhancements of STEREO EUVI emission flux) and photospheric magnetic events (as represented by the enhancements of SOHO MDI line of sight magnetic flux), when the populations in the two solar regions are matched by appropriate thresholds. We found that the event measures integrated

over space and time (the swept area S , the spatiotemporal volume V , and the integrated flux E) are described by essentially the same probability distribution functions, yielding the same values of the power-law exponents τ_S , τ_V , and τ_E for the photosphere and corona. The event measures that do not involve spatiotemporal integration show greater statistical discrepancies resulting in differing log-log slopes for the two solar regions. Likewise, the geometric exponents describing power-law relations between the measured parameters and the linear size L of the event also have distinct values. The analysis of scaling relations between the obtained scaling indices has shown that the probabilistic behavior of the MDI and EUVI events is consistent with their characteristic spatiotemporal geometries and indicates a strong physical interaction between the photosphere and corona. The derived scaling laws are in an agreement with the classical model in which the photospheric flux tubes undergo quasi one-dimensional horizontal convective motions driven by uncorrelated, random walk - like displacements which energize the corona in a multiscale fashion resulting in the power-law distribution of solar flares.

Until now, the multiscale behavior of coronal dissipation has been considered in frames of two alternative statistical-physical frameworks. The first framework, self-organized criticality, seeks to explain power-law distributions of flare parameters via cooperative interactions of a large number of nonlinearly coupled degrees of freedom representing unstable coronal loops and/or loop strands. If the interaction time scale is significantly shorter than the time scale characterizing photospheric motions, the interaction leads to scale-free avalanches of energy dissipation indicating that the system resides in the vicinity of a global critical state. The SOC behavior is robust with respect to the changes in microscopic physics: the same scaling laws are expected for different instability mechanisms as long as the critical dynamics remains in the same universality class (Sethna et al. 2001). This property of SOC model can be invoked to explain statistical universality of different classes of flares.

The second well-developed concept is the high-Reynolds number fluid turbulence. It has been proposed that multiscale energy release in the

corona could result from a turbulent intermittency (strongly inhomogeneous energy dissipation) associated with energy cascade in the corona (Boffetta et al. 1999; Nigro et al. 2004). In this framework, energy injection at the largest scale is due to photospheric motions whereas nonlinear effects in the corona are responsible for transferring the energy to ever smaller scales, similarly to the generation of multiscale eddies in turbulent fluids. Up to the accuracy of the available instrumentation, both SOC and turbulence are in an agreement with the observed scaling laws hinting at a possibility of a more universal phenomenology (Uritsky et al. 2007).

An important underlying assumption shared by the two concepts is that the photosphere plays a role of a “structureless” driver, with the observed hierarchy of scales generated self-consistently at the coronal altitudes. Both groups of models are largely insensitive to the driving conditions as long as the scale separation requirements mentioned above are met.

The results of this study lead to a drastically different interpretation which seems to be much simpler. We presented a case suggesting that it is the multiscale photospheric motion, and not a complicated intrinsic process in the corona such as SOC or turbulence, that shapes the statistical distribution of solar flares, at least for a quiet Sun. In other words, the coronal flaring activity has a multiscale spatiotemporal pattern *because the free energy input from the photosphere is fragmented into multiscale packets with a matching power-law probability distribution of sizes*. The Occam’s razor principle requires that among competing hypotheses, it is justified to pick the one which makes the fewest assumptions. Following this principle, the direct interaction between the two solar regions should be preferred.

The proposed mechanism of multiscale probabilistic coupling is in a good quantitative agreement with scaling properties of the estimated free magnetic energy supplied to the corona by the photospheric shuffling and/or through an excitation of multiscale Alfvén wave packets as shown in section 3.4. Each successful shuffling event generating a positive line of sight Poynting flux sends a packet of free energy into the corona via a multitude of DC and/or AC coupling mechanisms (see e.g. Davila (1987); Ofman et al.

(1994); Ofman & Davila (1995); Klimchuk (2006); McIntosh et al. (2011)). According to our analysis, the amount of the injected free energy follows a power-law distribution described by the same log-log slope as the distribution of the integrated emission flux in the corona. It is worth mentioning that the wave coupling scenario can reach far beyond the corona and directly affect the acceleration and heating of the solar wind (see e.g. Ofman 2010). In this context, it would be important to investigate in future studies how the multiscale structure and dynamics of the solar photosphere are imprinted in the solar wind turbulence.

It should be also noted that our conclusions apply to relatively strong coronal dissipation events due to the thresholding which eliminated most of the small-scale flares. Generally, any threshold-based technique introduces an ambiguity with regards to the sizes of the detected features: the lower the threshold, the larger is the apparent size. The threshold dependence is especially strong when the probability density function of the measured parameter exhibits a slow non-exponential decay as is the case with the distributions of MDI and EUVI pixel counts (see Fig. 3). Since the events were selected by applying rather high intensity thresholds tuned to intermittent spikes in the studied images, the actual physical dimensions of the events in our analysis could significantly exceed the estimated values. Therefore, our statistics are likely to describe relatively large events produced by strong magnetic discontinuities and involving considerable plasma volumes, possibly on multiple interwoven coronal loops. For smaller events occurring inside individual loops, the photospheric length scales are obviously not be directly “transferred” because the magnetic field strength decreases by orders of magnitude from the photosphere to the corona, and the transverse scale expands accordingly. The multiscale dissipation pattern appearing at these scales must build up in the corona independently of the photospheric structure, e.g. following SOC and/or turbulence scenarios.

In summary, the conducted analysis strongly suggests that energy dissipation scales of coronal heating events can be directly controlled by turbulent photospheric convection. Our findings speak in favor of the coupling scenario proposed by Parker (Parker 1983, 1988) in which random

photospheric shufflings generate marginally stable magnetic discontinuities at the coronal level. They are also consistent with the the Alfvén wave heating mechanism (Davila 1987; Ofman et al. 1998; De Pontieu et al. 2007) which can play a major part at shorter time scales. Subsequently, coronal instabilities relax a subset of unstable magnetic structures or Alfvénic wave packets repeating their probabilistic patterns. The value of the energy distribution exponent ($\hat{\tau}_E \sim 1.5$) resulting from this coupling is too low for the smallest dissipation events to play a prevailing role in the coronal heating process. The large-scale processes such as those driven by the mesogranulation flow are likely to be releasing a dominant portion of free magnetic energy dissipated in the corona, at least for the range of coronal emission intensities considered in our study. The question remains: is this energy sufficient to provide the bulk coronal heating necessary for the observed radiative loss rates?

We would like to thank J. Klimchuk and M. Aschwanden for useful discussions and advice. The work of V.U. was supported by the NASA grant NNG11PL10A 670.002 through the CUA’s Institute for Astrophysics and Computational Sciences. LO was supported by NASA grant NNX12AB34G.

REFERENCES

- Abramenko, V. I. 2005, *Astrophysical J.*, 629, 1141
- Abramenko, V. I., & Yurchyshyn, V. B. 2010, *Astrophysical J.*, 722, 122
- Abramenko, V. I., Yurchyshyn, V. B., Wang, H., Spirock, T. J., & Goode, P. R. 2002, *Astrophysical J.*, 577, 487
- Antiochos, S. K. 1998, *Astrophysical J.*, 502, L181
- Antiochos, S. K., DeVore, C. R., Karpen, J. T., & Mikic, Z. 2007, *Astrophysical J.*, 671, 936
- Aschwanden, M. J. 2006, *Physics of the solar corona* (Berlin Heidelberg: Springer-Verlag)
- . 2011, *Self-organized criticality in astrophysics* (Berlin Heidelberg: Springer-Verlag)
- . 2012a, *Astrophysical J.*, 757, 94
- . 2012b, *Astronomy and Astrophysics*, 539, A2
- Aschwanden, M. J., ed. 2013, *Self-Organized Criticality Systems* (Open Academic Press GmbH & Co.)
- Aschwanden, M. J., Nightingale, R. W., Tarbell, T. D., & Wolfson, C. J. 2000a, *Astrophysical J.*, 535, 1027
- Aschwanden, M. J., & Parnell, C. E. 2002, *Astrophysical J.*, 572, 1048
- Aschwanden, M. J., Tarbell, T. D., Nightingale, R. W., Schrijver, C. J., Title, A., Kankelborg, C. C., Martens, P., & Warren, H. P. 2000b, *Astrophysical J.*, 535, 1047
- Athay, R. G. 1966, *Astrophysical J.*, 146, 223
- Baiesi, M., Paczuski, M., & Stella, A. L. 2006, *Phys. Rev. Lett.*, 96, 051103
- Bak, P., Tang, C., & Wiesenfeld, K. 1987, *Phys. Rev. Lett.*, 59, 381
- . 1988, *Phys. Rev. A*, 38, 364
- Balke, A. C., Schrijver, C. J., Zwaan, C., & Tarbell, T. D. 1993, *Solar Phys.*, 143, 215
- Barabási, A.-L., & Stanley, H. E. 1995, *Fractal concepts in surface growth* (Cambridge, UK: Cambridge Univ. Press)
- Berger, T. E., Lofdahl, M. G., Shine, R. S., & Title, A. M. 1998, *Astrophysical J.*, 495, 973
- Berger, T. E., & Title, A. M. 1996, *Astrophysical J.*, 463, 365
- Berghmans, D., & Clette, F. 1999, *Solar Phys.*, 186, 207
- Berghmans, D., Clette, F., & Moses, D. 1998, *Astronomy and Astrophysics*, 336, 1039
- Biham, O., Milshtein, E., & Malcai, O. 2001, *Phys. Rev. E*, 63, 061309
- Biskamp, D. 2003, *Magnetohydrodynamic turbulence* (Cambridge, UK: Cambridge Univ. Press)
- Boffetta, G., Carbone, V., Giuliani, P., Veltri, P., & Vulpiani, A. 1999, *Phys. Rev. Lett.*, 83, 4662
- Bouchaud, J. P., & Georges, A. 1990, *Phys. Reports – Review Section Phys. Lett.*, 195, 127

- Cadavid, A. C., Lawrence, J. K., Ruzmaikin, A. A., & Kaylengknight, A. 1994, *Astrophysical J.*, 429, 391
- Chang, T. 1992, *IEEE Transactions on Plasma Science*, 20, 691
- Chaouche, L. Y., et al. 2011, *Astrophysical J. Lett.*, 727, L30
- Charbonneau, P., McIntosh, S. W., Liu, H. L., & Bogdan, T. J. 2001, *Solar Phys.*, 203, 321
- Conlon, P. A., McAteer, R. T. J., Gallagher, P. T., & Fennell, L. 2010, *Astrophysical J.*, 722, 577
- Corral, A., & Paczuski, M. 1999, *Phys. Rev. Lett.*, 83, 572
- Crosby, N. B. 2011, *Nonlinear Processes in Geophysics*, 18, 791
- Crosby, N. B., Aschwanden, M. J., & Dennis, B. R. 1993, *Solar Phys.*, 143, 275
- Crouch, A. D., Charbonneau, P., & Thibault, K. 2007, *Astrophysical J.*, 662, 715
- Davila, J. M. 1987, *Astrophysical J.*, 317, 514
- De Pontieu, B., et al. 2007, *Science*, 318, 1574
- DeForest, C. E., Hagenaar, H. J., Lamb, D. A., Parnell, C. E., & Welsch, B. T. 2007, *Astrophysical J.*, 666, 576
- Dmitruk, P., & Gomez, D. O. 1997, *Astrophysical J.*, 484, L83
- Espagnet, O., Muller, R., Roudier, T., & Mein, N. 1993, *Astronomy and Astrophysics*, 271, 589
- Falconer, D. A., Moore, R. L., & Gary, G. A. 2008, *Astrophysical J.*, 689, 1433
- Falconer, D. A., Moore, R. L., Porter, J. G., & Hathaway, D. H. 1998, *Astrophysical J.*, 501, 386
- Feder, J. 1988, *Fractals: Physics of Solids and Liquids* (New York: Springer-Verlag)
- Fuentes, M. C. L., & Klimchuk, J. A. 2010, *Astrophysical J.*, 719, 591
- Fujimura, D., & Tsuneta, S. 2009, *Astrophysical J.*, 702, 1443
- Georgoulis, M. K. 2005, *Solar Phys.*, 228, 5
- Grassberger, P., & Delatorre, A. 1979, *Annals Phys.*, 122, 373
- Howard, R. A., et al. 2008, *Space Science Rev.*, 136, 67
- Isichenko, M. B. 1992, *Rev. Modern Phys.*, 64, 961
- Jensen, H. J. 1998, *Self-organized criticality: Emergent complex behavior in physical and biological systems* (New York: Cambridge Univ. Press)
- Klimchuk, J. A. 2006, *Solar Phys.*, 234, 41
- Krucker, S., & Benz, A. O. 1998, *Astrophysical J.*, 501, L213
- Kudoh, T., & Shibata, K. 1999, *Astrophysical J.*, 514, 493
- Lamb, D. A., DeForest, C. E., Hagenaar, H. J., Parnell, C. E., & Welsch, B. T. 2008, *Astrophys. J.*, 674, 520
- Lawrence, J. K., Ruzmaikin, A. A., & Cadavid, A. C. 1993, *Astrophysical J.*, 417, 805
- Lu, E. T., & Hamilton, R. J. 1991, *Astrophysical J.*, 380, L89
- Mandelbrot, B. B. 1977, *Form, Chance, and Dimension* (San Francisco: W. H. Freeman)
- . 1982, *The fractal geometry of Nature* (New York: W. H. Freeman)
- Mandelbrot, B. B., & VanNess, J. W. 1968, *SIAM Rev.*, 10, 422
- McAteer, R. T. J., Gallagher, P. T., & Conlon, P. A. 2010, *Adv. Space Res.*, 45, 1067
- McIntosh, S. W., & Charbonneau, P. 2001, *Astrophysical J.*, 563, L165
- McIntosh, S. W., Pontieu, B. D., Carlsson, M., Hansteen, V., Boerner, P., & Goossens, M. 2011, *Nature*, 475, 477
- Metzler, R., & Klafter, J. 2000, *Phys. Reports – Review Section Phys. Lett.*, 339, 1
- Mitra-Kraev, U., & Benz, A. O. 2001, *Astronomy and Astrophysics*, 373, 318

- Monin, A. S., & Yaglom, A. M. 1975, Statistical fluid mechanics: Mechanics of turbulence, Vol. Vol. 2 (MIT Press)
- Morales, L., & Charbonneau, P. 2008, *Astrophysical J.*, 682, 654
- Munoz, M. A., Dickman, R., Vespignani, A., & Zapperi, S. 1999, *Phys. Rev. E*, 59, 6175
- Nigro, G., Malara, F., Carbone, V., & Veltri, P. 2004, *Phys. Rev. Lett.*, 92, 194501
- Ofman, L. 2010, *Living Rev. in Solar Phys.*, 7, 4
- Ofman, L., & Davila, J. M. 1995, *Astrophysical J.*, 444, 471
- Ofman, L., Davila, J. M., & Steinolfson, R. S. 1994, *Astrophysical J.*, 421, 360
- Ofman, L., Klimchuk, J. A., & Davila, J. M. 1998, *Astrophysical J.*, 493, 474
- Parker, E. N. 1983, *Astrophysical J.*, 264, 642
- . 1988, *Astrophysical J.*, 330, 474
- Parnell, C. E., DeForest, C. E., Hagenaar, H. J., Johnston, B. A., Lamb, D. A., & Welsch, B. T. 2009, *Astrophysical J.*, 698, 75
- Parnell, C. E., & Jupp, P. E. 2000, *Astrophysical J.*, 529, 554
- Rast, M. P. 2003, *Astrophysical J.*, 597, 1200
- Robinson, P. A. 1994, *Phys. Rev. E*, 49, 3919
- Scherrer, P. H., et al. 1995, *Solar Phys.*, 162, 129
- Schrijver, C. J., Zwaan, C., Balke, A. C., Tarbell, T. D., & Lawrence, J. K. 1992, *Astronomy and Astrophysics*, 253, L1
- Sethna, J. P., Dahmen, K. A., & Myers, C. R. 2001, *Nature*, 410, 242
- Shelyag, S., Mathioudakis, M., & Keenan, F. P. 2012, *Astrophysical J. Lett.*, 753, L22
- Sherbrooke, E. C., Patrikalakis, N. M., & Wolter, F. E. 1996, *Graphical Models Image Processing*, 58, 574
- Simon, G. W., Title, A. M., & Weiss, N. O. 1995, *Astrophysical J.*, 442, 886
- . 2001, *Astrophysical J.*, 561, 427
- Solanki, S. K., Inhester, B., & Schussler, M. 2006, *Reports on Progress in Phys.*, 69, 563
- Stolovitzky, G., & Sreenivasan, K. R. 1994, *Rev. Modern Phys.*, 66, 229
- Suzuki, T. K., & Inutsuka, S. 2006, *J. Geophysical Research – Space Phys.*, 111, A06101
- Török, T., Panasenco, O., Titov, V. S., Mikic, Z., Reeves, K. K., Velli, M., Linker, J. A., & Toma, G. D. 2011, *Astrophysical J. Lett.*, 739, L63
- Turcotte, D. L. 1989, *Pure Appl. Geophysics*, 131, 171
- . 1997, *Fractals and chaos in geology and geophysics* (Cambridge, UK: Cambridge Univ. Press)
- Ulrich, R. K. 1996, *Astrophysical J.*, 465, 436
- Uritsky, V. M., & Davila, J. M. 2012, *Astrophysical J.*, 748, 60
- Uritsky, V. M., Davila, J. M., & Jones, S. I. 2009, *Phys. Rev. Lett.*, 103, 039502
- Uritsky, V. M., Donovan, E., Trondsen, T., Pineau, D., & Kozelov, B. V. 2010a, *J. Geophysical Research – Space Phys.*, 115, A09205
- Uritsky, V. M., Klimas, A. J., & Vassiliadis, D. 2006, *Geophys. Res. Lett.*, 33
- Uritsky, V. M., Paczuski, M., Davila, J. M., & Jones, S. I. 2007, *Phys. Rev. Lett.*, 99, 025001
- Uritsky, V. M., Pouquet, A., Rosenberg, D., Mininni, P. D., & Donovan, E. F. 2010b, *Phys. Rev. E*, 82, 056326
- Vespignani, A., Dickman, R., Munoz, M. A., & Zapperi, S. 2000, *Phys. Rev. E*, 62, 4564
- Vespignani, A., & Zapperi, S. 1998, *Phys. Rev. E*, 57, 6345
- Viall, N. M., & Klimchuk, J. A. 2011, *Astrophysical J.*, 738, 24
- . 2012, *Astrophysical J.*, 753, 35
- Vlahos, L., & Georgoulis, M. K. 2004, *Astrophysical J.*, 603, L61

Vöglér, A., & Schüssler, M. 2007, *Astronomy and Astrophysics*, 465, L43

Welsch, B. T. 2006, *Astrophysical J.*, 638, 1101

Table 1: Percentile thresholds used to detect intermittent events in SOHO MDI and STEREO EUVI image sets (n - number of detected events).

p	MDI threshold	EUVI threshold
95.0 %	13.5 ($n = 38242$)	202 ($n = 4124$)
97.0 %	17.3 ($n = 19114$)	217 ($n = 3005$)
99.0 %	32.3 ($n = 5912$)	258 ($n = 1269$)
99.5 %	42.0 ($n = 3410$)	292 ($n = 686$)

Table 2: Scaling exponents of the detected photospheric and coronal events, as a function of the percentile threshold.

	MDI			EUVI		
x	D_x	τ_x	Δ_x	\hat{D}_x	$\hat{\tau}_x$	$\hat{\Delta}_x$
$p = 95\%$						
L	1.00 ± 0.00	3.93 ± 0.01	2.94	1.00 ± 0.00	2.68 ± 0.22	1.66
T	2.02 ± 0.17	2.31 ± 0.07	2.64	1.33 ± 0.09	2.12 ± 0.11	1.50
A	1.42 ± 0.03	2.99 ± 0.06	2.82	1.59 ± 0.03	2.03 ± 0.10	1.64
S	2.74 ± 0.16	2.06 ± 0.03	2.92	1.99 ± 0.04	1.86 ± 0.05	1.71
V	3.18 ± 0.19	1.92 ± 0.02	2.93	2.58 ± 0.09	1.64 ± 0.04	1.66
E	3.65 ± 0.20	1.80 ± 0.02	2.91	3.04 ± 0.05	1.50 ± 0.04	1.53
$p = 97\%$						
L	1.00 ± 0.00	3.67 ± 0.19	2.67	1.00 ± 0.00	2.45 ± 0.15	1.44
T	2.15 ± 0.09	2.00 ± 0.03	2.14*	1.38 ± 0.06	1.92 ± 0.09	1.27*
A	1.40 ± 0.02	2.80 ± 0.02	2.52	1.60 ± 0.03	1.82 ± 0.02	1.31
S	2.82 ± 0.13	1.91 ± 0.03	2.56	2.00 ± 0.03	1.80 ± 0.01	1.59*
V	3.32 ± 0.14	1.75 ± 0.03	2.49	2.61 ± 0.04	1.60 ± 0.04	1.57
E	3.77 ± 0.12	1.65 ± 0.03	2.46	3.07 ± 0.03	1.43 ± 0.04	1.31
$p = 99\%$						
L	1.00 ± 0.00	3.08 ± 0.03	2.12	1.00 ± 0.00	2.11 ± 0.17	1.08
T	2.21 ± 0.06	1.84 ± 0.04	1.84*	1.34 ± 0.14	2.04 ± 0.11	1.39*
A	1.34 ± 0.04	2.53 ± 0.03	2.06	1.60 ± 0.09	1.77 ± 0.13	1.23*
S	2.75 ± 0.09	1.79 ± 0.04	2.18	1.99 ± 0.01	1.75 ± 0.07	1.50*
V	3.39 ± 0.10	1.63 ± 0.04	2.15	2.63 ± 0.03	1.56 ± 0.06	1.47*
E	3.78 ± 0.10	1.52 ± 0.04	1.96	3.01 ± 0.02	1.47 ± 0.06	1.42*
$p = 99.5\%$						
L	1.00 ± 0.00	3.22 ± 0.35	2.30	1.00 ± 0.00	2.53 ± 0.01	1.54
T	2.14 ± 0.08	1.74 ± 0.03	1.58*	1.28 ± 0.04	2.32 ± 0.14	1.69
A	1.43 ± 0.01	2.50 ± 0.10	2.14	1.62 ± 0.11	1.78 ± 0.15	1.26*
S	2.81 ± 0.19	1.68 ± 0.03	1.90*	1.95 ± 0.03	1.86 ± 0.10	1.68
V	3.46 ± 0.21	1.49 ± 0.07	1.68*	2.60 ± 0.00	1.58 ± 0.07	1.51
E	3.82 ± 0.22	1.44 ± 0.04	1.68*	2.97 ± 0.06	1.58 ± 0.10	1.71

Table 3: Average values of scaling exponents obtained by combining $p = 99\%$ and 99.5% data for the photospheric events, $p = 95\%$ and 97% data for the coronal events. The distribution exponents of time-integrated parameters are highlighted with bold font.

x	D_x	\hat{D}_x	τ_x	$\hat{\tau}_x$	$\hat{\tau}_x$, predicted
L	1.00 ± 0.00	1.00 ± 0.00	3.15 ± 0.18	2.57 ± 0.13	2.55
T	2.18 ± 0.05	1.36 ± 0.05	1.79 ± 0.03	2.02 ± 0.07	1.91
A	1.39 ± 0.02	1.60 ± 0.02	2.52 ± 0.05	1.93 ± 0.06	1.95
S	2.78 ± 0.11	2.00 ± 0.03	1.74 ± 0.03	1.83 ± 0.03	1.74
V	3.43 ± 0.12	2.60 ± 0.05	1.56 ± 0.04	1.62 ± 0.03	1.56
E	3.80 ± 0.12	3.06 ± 0.03	1.48 ± 0.03	1.47 ± 0.03	1.42

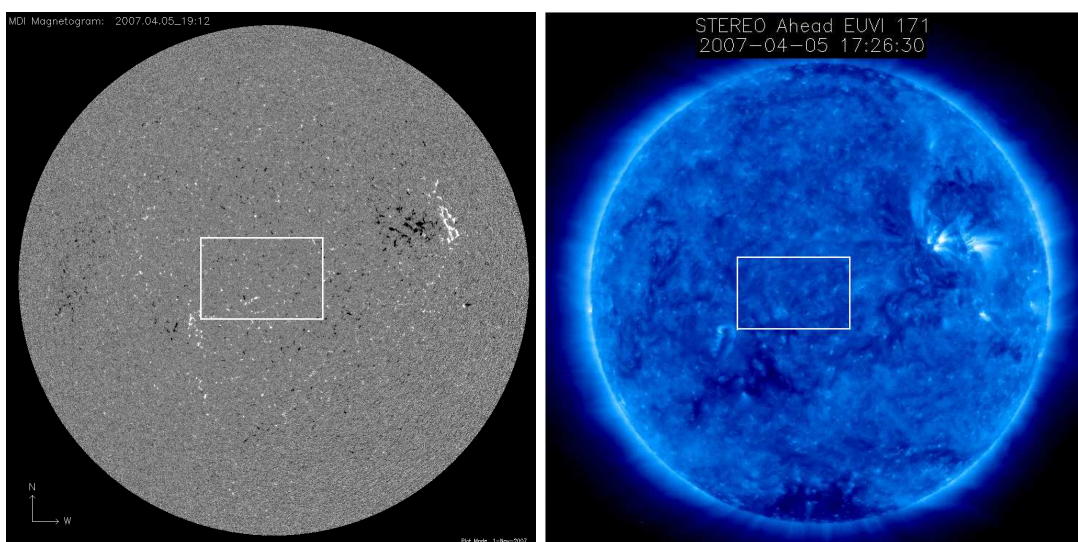


Fig. 1.— Full-disk SOHO MDI magnetogram (left) and STEREO EUVI image (right) showing the studied quiet solar region.

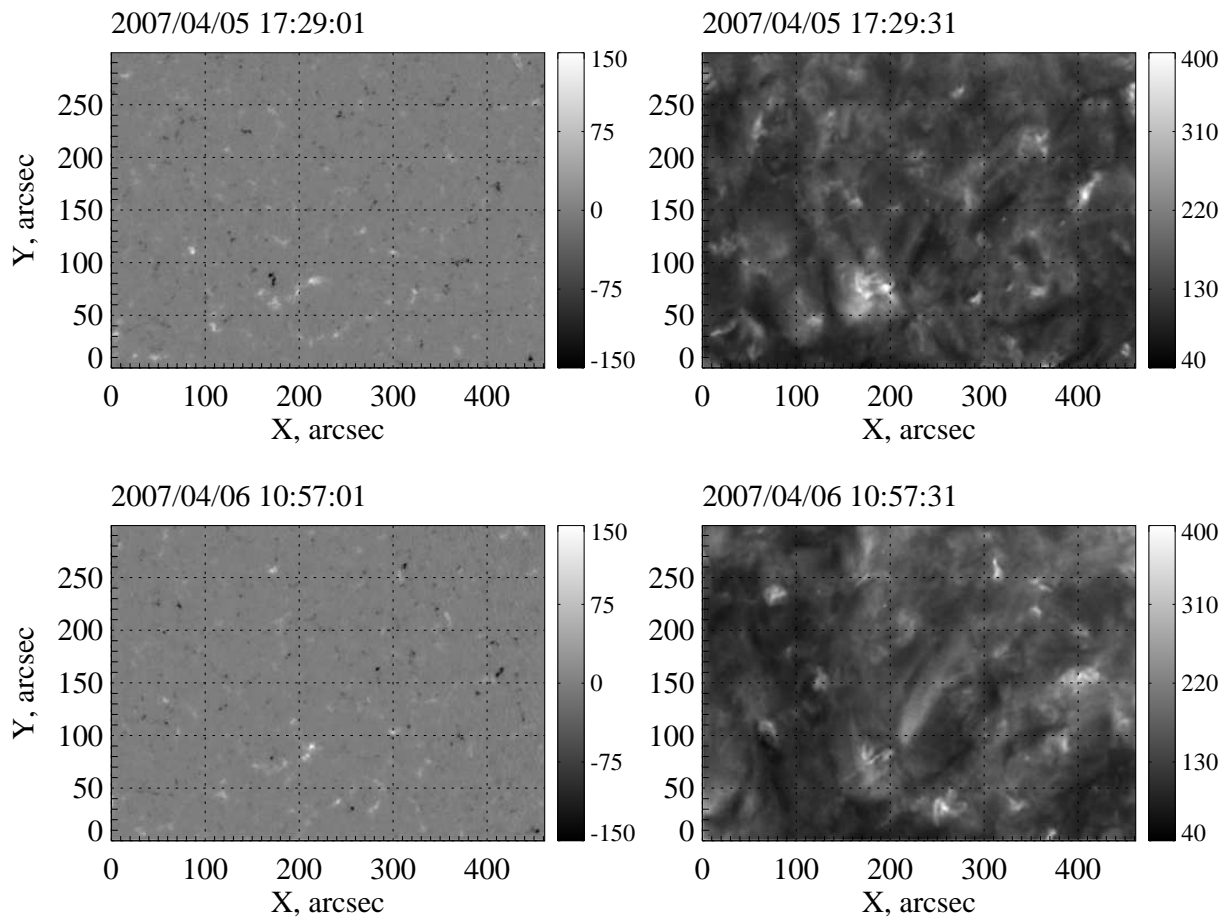


Fig. 2.— The first (top) and the last (bottom) images in the studied conjugate sets of SOHO MDI and STEREO EUVI observations (left and right columns, correspondingly).

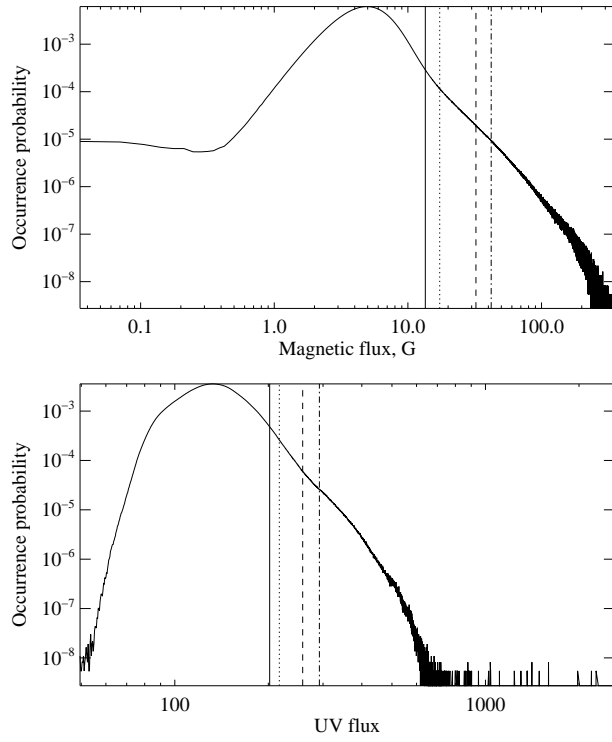


Fig. 3.— Probability distributions of MDI magnetic fluxes (top) and EUVI emission fluxes (bottom) describing the entire observational interval. Solid, dotted, dashed and dot-dashed vertical lines show respectively the percentile levels $p = 95.0, 97.0, 99.0$, and 99.5% used to detect intermittent events in each data set.).

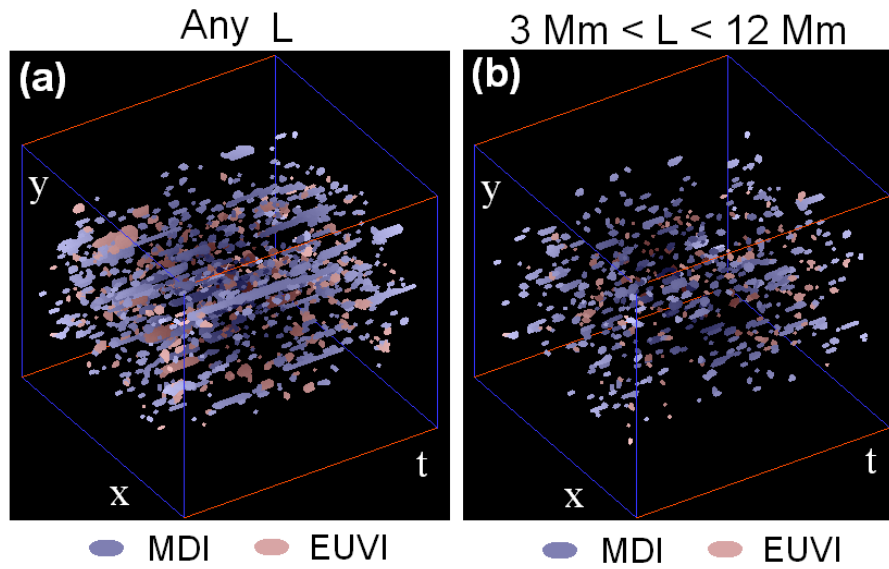


Fig. 4.— Spatiotemporal plots showing about 1/4 of the photospheric (MDI) and coronal (EUVI) events detected at respectively $p = 99\%$ and 95% percentile levels. (a) No restriction on the linear size L of the events is applied; (b) linear size is limited by the interval of scales $L \in (3, 12)$ Mm used for evaluating scaling exponents.

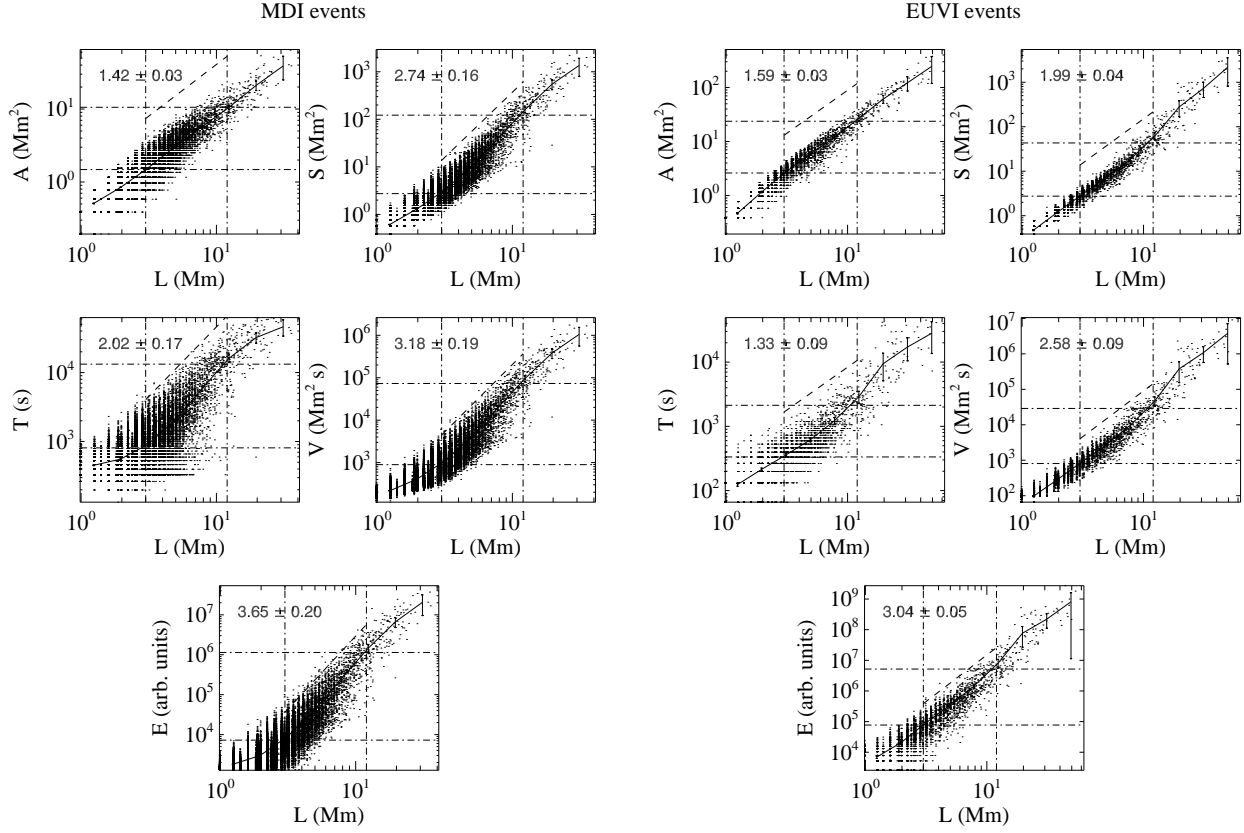


Fig. 5.— Scatterplots of photospheric magnetic enhancement events (left) and coronal emission events (right) detected respectively from SOHO MDI and STEREO EUVI images at the 95% percentile threshold.

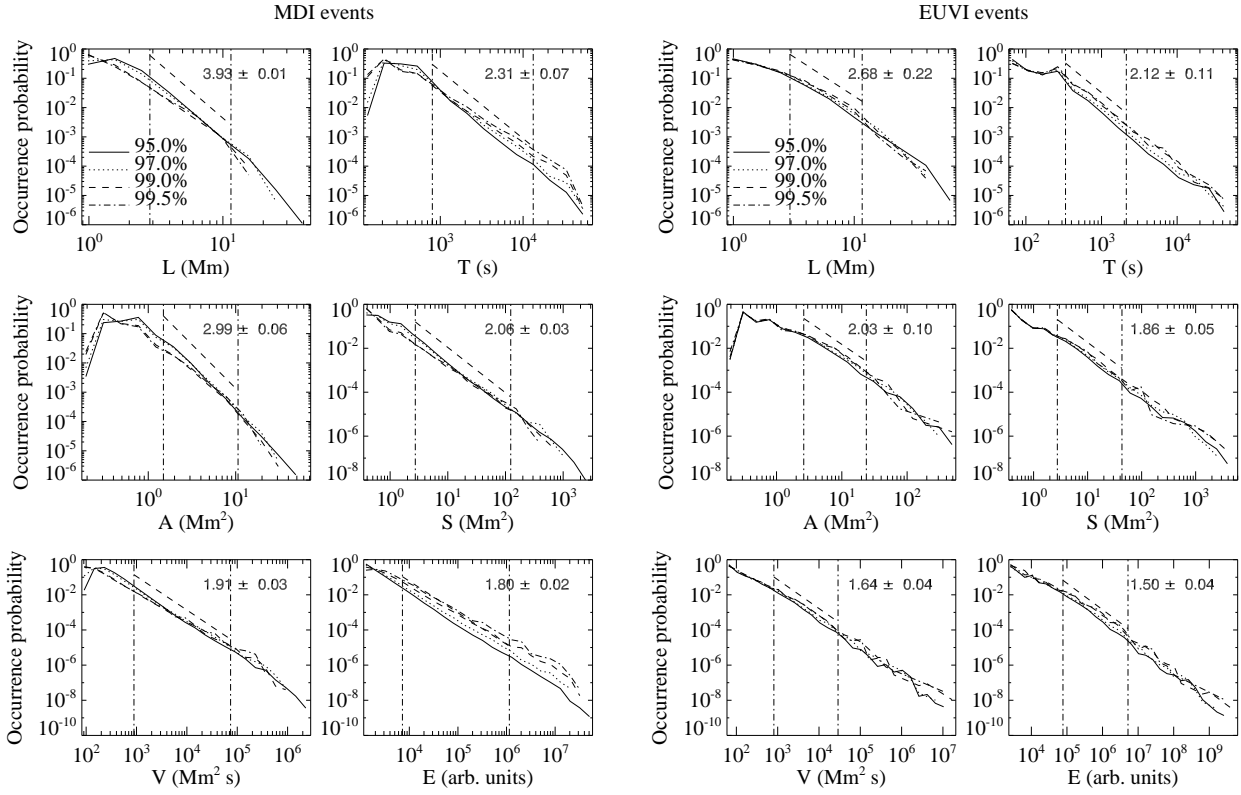


Fig. 6.— Probability distributions of the photospheric magnetic events (left) and the coronal emission events (right) detected respectively from SOHO MDI and STEREO EUVI images at four different percentile thresholds shown in Fig. 3.

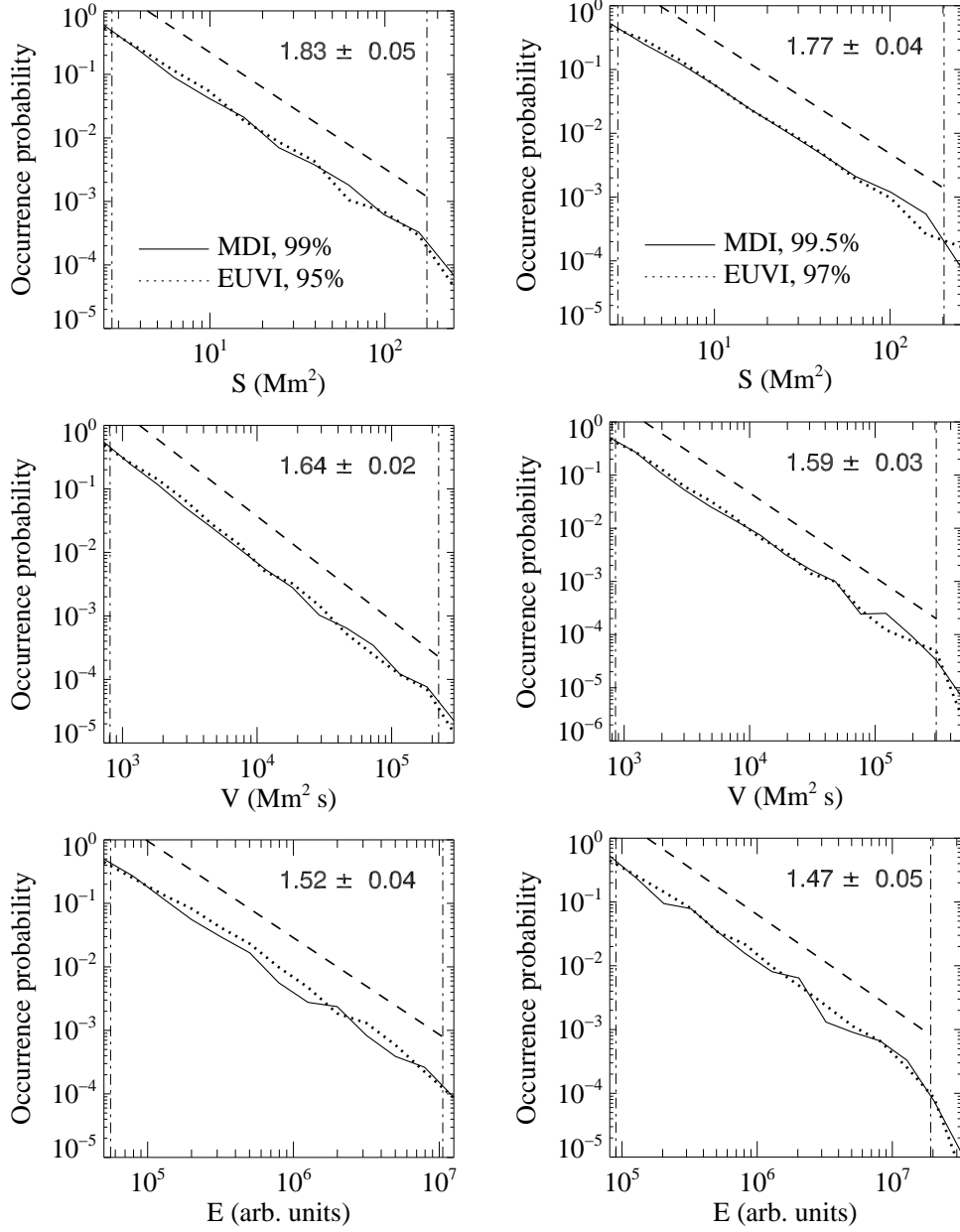


Fig. 7.— Comparison of probability distributions of photospheric and coronal events obtained for two combinations of thresholds yielding comparable numbers of detected events in each data sets. The slope values shown on each panel are the average log-log slopes for each pair of MDI and EUVI distribution evaluated over a combined range of scales defined by a union of the MDI and EUVI scaling ranges shown in Fig. 6(a) and (b) with vertical lines.

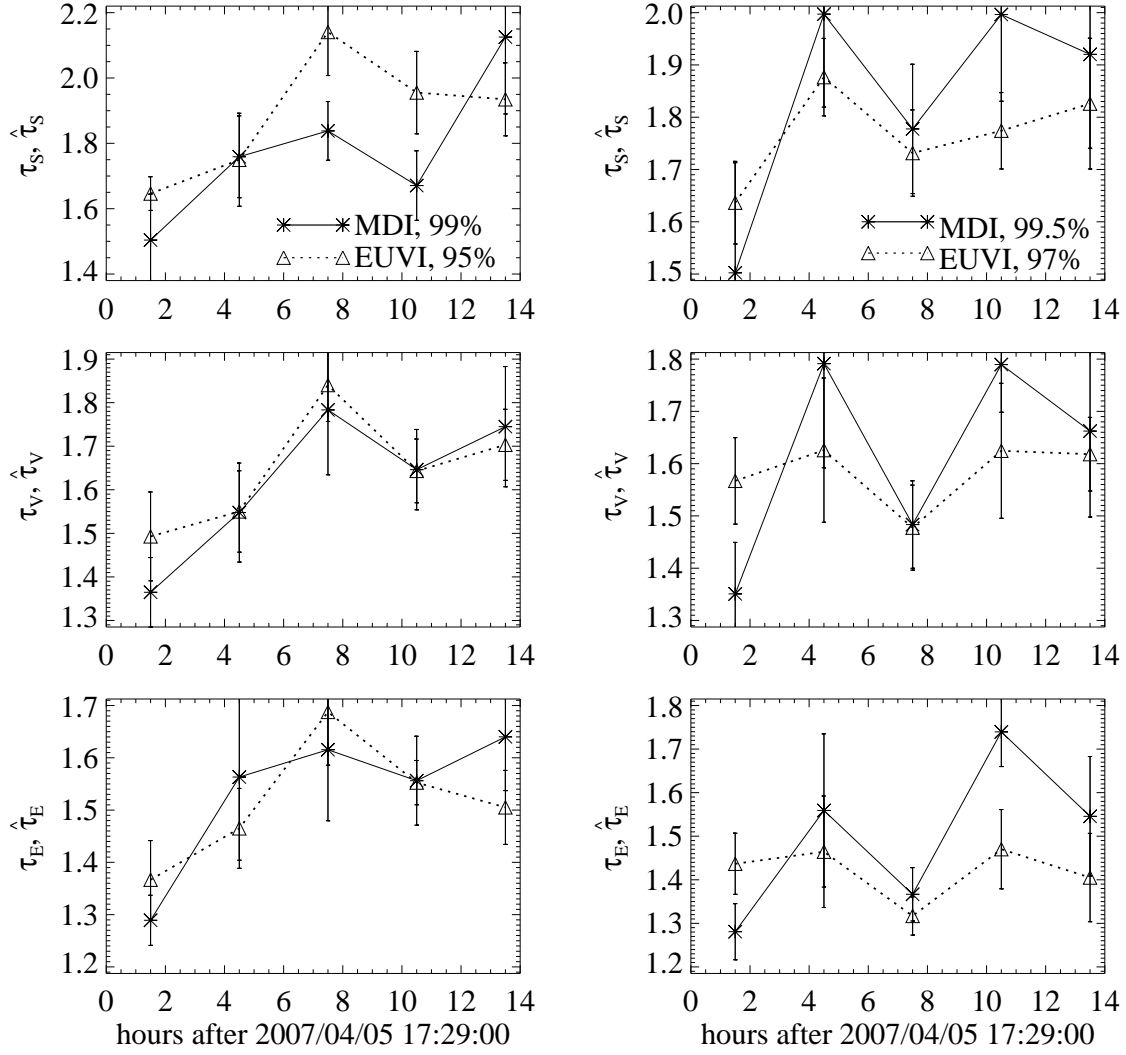


Fig. 8.— Temporal evolution of power-law probability distribution exponents of MDI and EUVI events computed within a 90-minute moving window. Vertical bars show the standard errors of the plotted power-law indices.

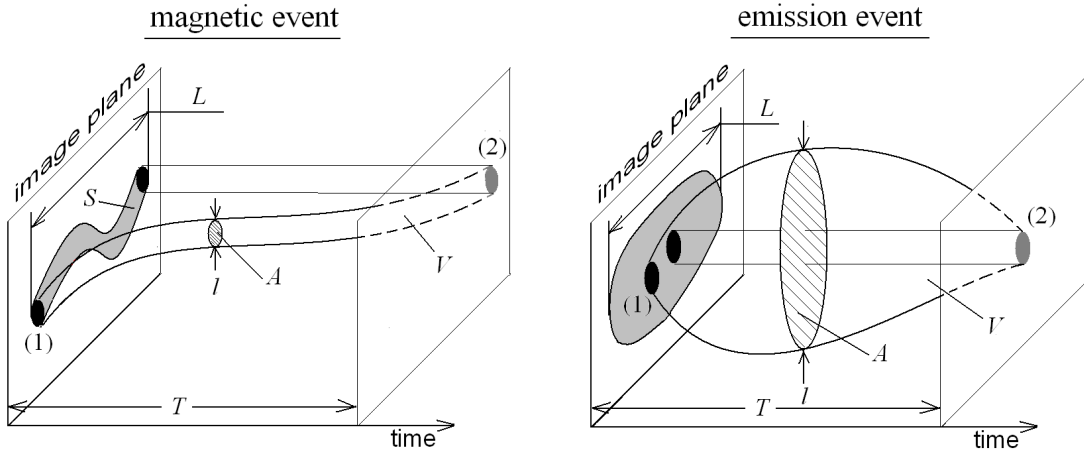


Fig. 9.— Schematic illustration of the characteristic spatiotemporal geometry of magnetic and emission events consistent with the conducted scaling analysis. Labels (1) and (2) refer respectively to the initial and final locations of the event; the shaded region is the projection of the event onto the image plane defining the swept area S .